Title: Huntingtin S421 phosphorylation increases kinesin and dynein engagement on early endosomes and lysosomes

Authors: Emily N. P. Prowse[1], Abdullah R. Chaudhary[1], David Sharon[1], Adam G. Hendricks[1]*

Affiliations: 1. Bioengineering Department, McGill University, Montreal, QC, Canada
Corresponding Author*: adam.hendricks@mcgill.ca

Key words: kinesin, dynein, huntingtin, intracellular transport

Summary Statement

Huntingtin phosphorylation at S421 increases the outward motility of early endosomes and lysosomes by enhancing the microtubule binding and force generation of kinesin and dynein.

ABSTRACT

Huntingtin (htt) acts as a scaffolding protein that recruits motor proteins to vesicular cargoes, enabling it to regulate kinesin- and dynein-dependent transport. To maintain the native stoichiometry of huntingtin with its interacting partners, we used CRISPR/Cas9 to induce a phosphomimetic mutation of the endogenous htt at S421 (S421Dhtt). Using single-particle tracking, optical tweezers, and immunofluorescence, we examined the effects of this mutation on the motility of early endosomes and lysosomes. In S421Dhtt cells, early endosomes and lysosomes exhibited more outward motility towards the cell periphery compared to wild-type (WT) cells. In contrast, overexpression of htt had variable effects on the processivity, run length, and directional bias of both early endosomes and lysosomes. Kinesins and dyneins exerted greater forces on early endosomes and lysosomes in cells expressing S421Dhtt. Additionally, endosomes had higher binding rates, increased resistance to detachment under load, and enhanced recruitment of kinesins and dyneins in S421Dhtt cells. These data indicate that phosphorylation of the endogenous huntingtin causes early endosomes and lysosomes to move towards the cell periphery by activating both kinesins and dyneins.

List of Symbols and Abbreviations

α	Processivity parameter alpha
BDNF	Brain derived neurotrophic factor
DIC	Dynein intermediate chain
Early	Early endosome
EGF-qdot	Epidermal growth factor coated quantum dot
HD	Huntington's Disease
Htt	Huntingtin
KHC	Kinesin heavy chain
ks	Kolmogorov-Smirnov statistical test
latA	Latrunculin A
NZ	Nocodazole
R_g	Radius of gyration
S421Ahtt	Phosphoresistive huntingtin with the mutation S421A
S421Dhtt	Phosphomimetic huntingtin with the mutation S421D
WT+S421Dhtt	WT cells overexpressing mCherry-S421Dhtt
WT	Wild-type
WT+WThtt	WT cells overexpressing mCherry-WThtt

INTRODUCTION

Huntingtin (htt) is an essential, multifunctional, and ubiquitous protein. It consists of several disordered regions and 34 α-helical HEAT repeats (Fig. 1A) (Guo et al., 2018). Htt is essential for embryonic development (Duyao et al., 1995; Nasir et al., 1995; Schmitt et al., 1995; Zeitlin et al., 1995), and is ubiquitously expressed in tissues including the brain, ovaries, and testis into adulthood (Li et al., 1993; Sharp et al., 1995). It has diverse roles within the cell, including regulation of gene expression (Dunah et al., 2002; Futter et al., 2009; Holbert et al., 2001; Li et al., 2002; Marcora et al., 2003; Zuccato et al., 2003), cell morphology (Lo Sardo et al., 2012; Thion et al., 2015), cell survival (Leavitt et al., 2006), and intracellular transport (Cason et al., 2021; Gauthier et al., 2004; Liot et al., 2013; Twelvetrees et al., 2010; Wong and Holzbaur, 2014). Htt enhances transport of brain derived neurotrophic factor (BDNF) vesicles (Gauthier et al., 2004; Zala et al., 2008), autophagosomes in the mid-axon (Cason et al., 2021; Wong and Holzbaur, 2014), TrkB signalling vesicles (Liot et al., 2013), and synaptic vesicles through $GABA_R$ signalling (Twelvetrees et al., 2010). The remarkable ubiquity and variety of htt's roles underscore the importance of understanding its function in health and disease.

Teams of kinesins and dyneins transport signalling and degradative cargoes. There are multiple kinesins that drive outward transport towards microtubule plus ends at the cell periphery. Different ratios of kinesin-1, kinesin-2, and kinesin-3 associate with distinct cargo populations, allowing different motility characteristics for each population of vesicles (Bentley et al., 2015). Each type of kinesin has a unique binding rate and velocity, which leads combinations of motors to create a motility barcode for cargoes. Unlike kinesins, there is only one form of cytoplasmic dynein that drives organelle transport. Dynein forms a complex with dynactin and activating adaptors such as BicD, Hook1, and others to direct inward transport towards microtubule minus ends at the cell center (Cason et al., 2021; McKenney et al., 2014; Schlager et al., 2014). Scaffolding and adaptor proteins work together to regulate the recruitment and activity of both kinesin and dynein motors on each cargo based on its identity.

Huntingtin recruits teams of kinesin, dynein, and myosin VI motors to cargoes, allowing it to control the cargo's direction of movement along microtubules and switching between actin and microtubules (Caviston et al., 2011). Htt interacts with molecular motors indirectly through adaptors; kinesin-1 and the dynein adaptor dynactin interact with htt through HAP1 (Engelender, 1997; Li et al., 1998; McGuire et al., 2006; Twelvetrees et al., 2010), and myosin VI interacts through optineurin (Sahlender et al., 2005). In addition, dynein interacts directly with htt through its intermediate chain, suggesting a prominent role for htt in regulating inward transport (Caviston et al., 2007). Htt's interaction with myosin VI suggests htt regulates transitions to the actin cytoskeleton for short range transport or tethering. Upon htt deletion or mutation, intracellular transport of many vesicular cargoes is severely inhibited (Caviston and Holzbaur, 2009; Hilditch-Maguire, 2000).

Polyglutamine expansion mutations in htt lead to Huntington's disease (HD), disrupting multiple cellular functions and leading to neurodegeneration in medium spiny neurons of the striatum (Gil and Rego, 2008). HD mutations cause htt to form novel interactions. Notably, through increased self-association mutant htt forms aggregates throughout the cytoplasm and nucleus (Davies et al., 1997). These interactions cause aberrant initiation of autophagy, mTOR signalling, mitochondrial fission, and palmitoylation (reviewed in Wanker et al., 2019). Additional defects occur in neuronal transcription, endoplasmic reticulum homeostasis, mitochondrial function, calcium signalling, synaptic activity, and intracellular transport (reviewed in Saudou and Humbert, 2016), demonstrating the importance of htt's native interaction network in maintaining homeostasis (Colin et al., 2008; Lemarié et al., 2021; Zala et al., 2008).

Huntingtin is regulated by multiple post-translational modifications, including palmitoylation, phosphorylation, sumoylation, ubiquitination, and acetylation. The functions and mechanisms of many of these modifications remain unknown. Its palmitoylation site at C214, regulated by HIP14 in the Golgi, facilitates interactions with vesicular membranes (Yanai et al., 2006). Palmitoylation is reduced in cells expressing the polyglutamine-expanded htt protein that leads to HD, while restoring palmitoylation

reduces aggregation and cytotoxicity in vitro (Lemarié et al., 2021). Sumoylation sites may contribute to nuclear import and transcriptional regulation (Steffan et al., 2004). Ubiquitination and acetylation regulate huntingtin-mediated autophagy (Wong and Holzbaur, 2014). Htt has 40 known phosphosites, many of which have unknown biological functions (reviewed by Saudou and Humbert, 2016). The phosphorylation state of serine 421 affects axonal transport direction and velocity of BDNF vesicles and autophagosomes (Colin et al., 2008; Wong and Holzbaur, 2014), while mitochondrial transport is unaffected by this phosphosite (Xu et al., 2020). Each of htt's post-translational modifications contribute to its role in transport of both signaling and degradative cargoes. Further, post-translational modifications are reduced in HD, disrupting the balance of htt's interactions with its binding partners (Colin et al., 2008; Lemarié et al., 2021; Zala et al., 2008).

Post-translational modifications of scaffolding proteins can influence transport direction. The phosphomimetic mutation (S421Dhtt) mimics a constitutively phosphorylated amino acid and biased BDNF transport towards the cell periphery, while phosphoresistive mutations (S421Ahtt) led to increased transport towards the cell center (Colin et al., 2008). The S421Dhtt mutation is neuroprotective in cells with the mutation that leads to HD (Zala et al., 2008), which motivates our attempt to understand the native role of this phosphosite in cells with normal (WT) htt. It has also been generalized for various scaffolding proteins including RILP, Miro/TRAK1/TRAK2, JIP1, JIP3/4 that post-translational modifications can modify transport direction (Fu and Holzbaur, 2014). These studies suggest that huntingtin phosphorylation directs transport towards the cell periphery.

To elucidate the effects of S421 phosphorylation at native expression levels and determine the mechanisms of regulation for both early endosomes and lysosomes, we applied CRISPR-based gene editing and single-molecule biophysics. Previous studies analyzed the motility of cargoes overexpressing S421Dhtt or S421Ahtt constructs and performed Western blotting to determine S421's role in transport regulation (Colin et al., 2008; Zala et al., 2008). Western blot and immunofluorescence in overexpressing COS7

cells suggests that S421 phosphorylation increases the recruitment of kinesin to cargoes (Colin et al., 2008; Zala et al., 2008). However, only a subset of the motors bound to a cargo might be active (Encalada et al., 2011). In addition, the critical stoichiometry of interactions between scaffolding proteins and motors is disrupted in overexpression systems. We generated an endogenous mutation to replicate htt's native interactions and expression levels and observed its effect on organelle transport. We measured the forces generated by the motors driving early endosome and lysosome transport with optical tweezers to determine whether phosphorylation of huntingtin modifies motor activity. Single particle tracking allowed us to obtain nanometer-resolution tracking of cargo motility. Combining single-molecule biophysical approaches with gene editing provided mechanistic insight into htt's regulation of intracellular transport by S421 phosphorylation.

To understand how S421 phosphorylation of htt regulates intracellular transport, we examined early endosome and lysosome transport in CRISPR-generated S421Dhtt HEK293T cells. Motility assays demonstrated an increase in outward (microtubule plus-ended) motility for both early endosomes and lysosomes in cells expressing S421Dhtt. Additionally, lysosome run length increased upon S421 phosphorylation. Examining the forces generated by microtubule motors on early endosomes and lysosomes, we observed both kinesin and dynein motors had higher binding rates and increased resistance to unbinding under load with S421Dhtt for both cargoes. Cells with S421Dhtt showed higher forces in both outward and inward directions on both early endosomes and lysosomes. A higher fraction of kinesins and dyneins associated to microtubules upon S421 phosphorylation. The phosphorylation-induced change in directional bias and force generation for lysosomes was more subtle than those for early endosomes. We hypothesize that the native motility characteristics of the cargoes dictate the effect of S421 phosphorylation on htt: inward-directed early endosomes become bidirectional while bidirectional lysosomes increase their displacement. Our data indicates phosphorylation of htt at S421 increases motor recruitment and activity of early endosomes and lysosomes. Additionally, overexpression of WT and S421D htt suggests overexpressed htt disrupts the transport complex of htt, motors, and adaptors required for transport, affecting cargo run length, processivity, and direction.

RESULTS

Endogenous S421D mutation does not affect cytoskeletal organization or huntingtin localization

Introducing a phosphomimetic S421D mutation in the endogenous huntingtin did not alter huntingtin expression levels and localization or the organization of the cytoskeleton and golgi. In generating the S421D HEK293T cell line, we aimed to preserve the native expression levels and stoichiometry of interactions between htt and its many interactors. We used a lentiviral CRISPR cassette to generate this S421D point mutant cell line (Fig. 1B) and identified a single positive clone with the desired mutation using next-generation sequencing (Fig. 1C). S421Dhtt did not result in appreciable changes to the actin nor microtubule morphology (Fig. 1D). To determine whether S421Dhtt caused major defects in dynein function, we probed the organization of the Golgi apparatus (Burkhardt et al., 1997; Caviston et al., 2007; Corthésy-Theulaz et al., 1992). We observed no changes in the percentage of cells with organized versus dispersed Golgi, indicating dynein function was not severely disrupted (Fig. 1E). Importantly, the S421D mutation did not affect huntingtin's localization nor expression level (Fig. 1F, G). Overexpression of mCherry-WThtt or mCherry-S421Dhtt leads to elevated expression of both constructs at similar levels (Fig. 1G). In iPSC-derived neurons expressing polyglutamine-expanded huntingtin (180Q), S421Dhtt led to increased mitochondrial surface area while the number of mitochondria remained similar (Xu et al., 2020). Immunofluorescence of the mitochondria in HEK293T cells showed a decrease in the mitochondrial number and area upon S421D mutation (Fig. 1H-J), suggesting that S421Dhtt mitochondrial regulation may be cell-type dependent. Together, immunofluorescence and huntingtin expression level characterization demonstrated that the S421D mutation did not substantially alter the cytoskeleton, Golgi apparatus, nor localization of huntingtin while mitochondrial morphology was affected.

Huntingtin phosphorylation directs early endosomes towards the cell periphery

156 Introducing the S421D phosphomimetic mutation in the endogenous huntingtin gene
157 induced an outward directional bias in early endosomes but did not alter run length nor
158 processivity. We hypothesized that the processivity, run length, and fraction of outwardly-
159 directed early endosomes would increase upon S421 phosphorylation based on previous
160 work with BDNF vesicles in neurons (Colin et al., 2008). We quantified the processivity of
161 organelle trajectories using the slope of the log-log plot of mean-squared displacement
162 (α). For cargoes transported by microtubule-based motor proteins, we expect that α >1 is
163 indicative of directed transport, while α = 1 indicates diffusive motion. The radius of
164 gyration (R_g) is an indicator of run length that determines the average position of a
165 trajectory and measures a radius containing half of the points in the trajectory from its
166 average position. We transfected cells with Rab5-eGFP to label early endosomes for
167 particle tracking (Fig. 2A, C and Movies S1, S2). The endogenous S421D mutation
168 increased the outward motility of early endosomes towards the cell periphery without
169 changing their processivity or run length (Fig. 2E, F, I). The outward directional bias was
170 previously described when truncated WThtt and S421Dhtt were overexpressed in primary
171 neurons (Colin et al., 2008; Zala et al., 2008). To dissect the effects of htt phosphorylation
172 and expression levels, we transiently transfected full length mCherry-WThtt (WT+WThtt)
173 or mCherry-S421Dhtt (WT+S421Dhtt). These transfections lead to a ~4-10-fold increase
174 in htt expression (Fig. 1G). Overexpression of S421Dhtt increased the processivity, run
175 length, and unexpectedly induced inward motility of early endosomes (Fig. 2E, F, I).
176 Interestingly, overexpression of WThtt increased the outward motility of early endosomes
177 (Fig. 2I). These unexpected results in overexpression conditions may be due to the
178 change in stoichiometry of htt's interactions with its native binding partners. The gene
179 edited S421D HEK293T cells demonstrate an outward bias of early endosomes, while htt
180 overexpression alters motility. This indicates that S421 phosphorylation is either recruiting
181 additional kinesins on early endosomes or increasing the activity of the kinesins present
182 on the early endosome.
183
184 **S421D increases run length and outward bias of lysosomes**
185

186 S421 phosphorylation increased lysosome run lengths and directed them toward the cell
187 periphery. We hypothesized S421Dhtt's effects to be universal for all htt-associated
188 cargoes, and therefore expected increased outward bias, processivity, and run length in
189 lysosomes. This hypothesis is supported by previous work showing that htt promotes
190 outward motility in the mid-axon of neurons for autophagosomes, which eventually mature
191 into lysosomes (Cason et al., 2021; Wong and Holzbaur, 2014). In both WT and S421D
192 experiments, the raw trajectories demonstrated the expected bidirectional motility (Fig.
193 2B, D and Movies S3, S4). S421Dhtt induced an increase in run length and outward
194 motility of lysosomes, without affecting their processivity (Fig. 2G, H, J). When we
195 overexpressed htt, we observed a minor increase in processivity for WThtt and a
196 substantial increase in run length regardless of the phosphorylation state (Fig. 2G, H, J).
197 Unexpectedly, WThtt overexpression led to an inward directional bias (Fig. 2J), while
198 overexpression of S421Dhtt reversed the effect by increasing outward motility. Taken
199 together, our results indicate that htt overexpression modifies processivity, run length,
200 and directional bias while phosphorylation shifts lysosome motility towards the cell
201 periphery and increases their run length. This suggests S421 phosphorylation at native
202 expression levels is increasing the number of active kinesin motors, as was observed for
203 early endosomes.
204
205 **Tethering on actin contributes to the directional bias of early endosomes**
206
207 Our results suggest that huntingtin's phosphorylation state modulates transient actin
208 tethering and contributes to the transport direction of early endosomes. Huntingtin
209 interacts with optineurin, which recruits myosin VI and could regulate cargo association
210 to actin (Sahlender et al., 2005). We used latrunculin A (latA) to depolymerize actin
211 filaments and reduce cargo association with actin. We expected an increase in run length
212 and processivity upon latA treatment since cargo tethering and confinement by actin are
213 reduced, allowing long range, processive motility by microtubule motors to dominate. We
214 determined the optimal concentration for motility assays via imaging cells labelled with
215 SiR-actin. We determined 250 nM latA was optimal as it resulted in significant
216 depolymerization of actin filaments without loss of native cellular morphology (Fig. S1A).

217 As expected, treatment with latA increased run length and processivity of Rab5 early
218 endosomes (Fig. S1B, C). Additionally, the phosphorylation-induced directional bias
219 became less prominent with latA, suggesting that short-range actin-based motility
220 contributes to the observed directional bias of early endosomes (Fig. S1D). WT early
221 endosomes have increased outward motility upon latA treatment, indicating that allowing
222 kinesin and dynein to dominate transport biases it outwards (Fig. S1D). The S421D
223 mutation did not further shift the directional bias in actin-depleted cells, suggesting that
224 both loss of actin tethering and htt phosphorylation act through similar mechanisms.
225
226 **Lysosomes have a higher dependence on microtubule-based transport**
227
228 Depolymerization of microtubules demonstrated no significant changes in processivity or
229 run length for early endosomes, while lysosomes showed significant decreases in both
230 run length and processivity. We used 10 μM nocodazole (NZ) to depolymerize
231 microtubules and observe how strongly the motility parameters were affected. We
232 expected that upon NZ treatment, both processivity and run length would decrease
233 because microtubule-based motors drive the long range processive transport of both
234 early endosomes and lysosomes. We observed this expected decrease in run length and
235 processivity for lysosomes, suggesting that they rely heavily on microtubule-based
236 transport to drive their motility (Fig. S1F, I, J). The large change in processivity and run
237 length for lysosomes demonstrates the magnitude of changes in these parameters upon
238 large scale disruption of the cytoskeleton. Early endosomes demonstrated a surprising
239 lack of effect of nocodazole treatment on their processivity and run length, perhaps due
240 to their inherently low processivity and run lengths compared to lysosomes (Fig. S1E, G,
241 H). The lysosomes in NZ-treated cells reached similar values for processivity and run
242 length to the early endosomes in the control condition, suggesting that the values for early
243 endosome motility were close to their minimum. Combining this result with our
244 conclusions from the latA treatment demonstrates that early endosome transport may be
245 more dependent on switching between actin-based and microtubule-based transport (Fig.
246 S1). These results indicate early endosome transport has a lower dependence on

247 microtubules compared to lysosomes, perhaps due to its inherently short run lengths and
248 lower processivity.
249
250 **S421 huntingtin phosphorylation activates kinesins and dyneins on early**
251 **endosomes**
252
253 To determine how changes in motor activity contribute to the motility we observed, we
254 measured the force generation of motors on early endosomes with optical tweezers. We
255 incubated cells with fibronectin-coated 500 nm polystyrene beads for 10-50 mins (Blocker
256 et al., 1997) and used optical tweezers to measure the forces that motors exerted in living
257 cells (Fig. 3A, B). At this stage of maturation, the early phagosomes (termed early
258 endosomes) are positive for Rab5 and other early endosome markers and represent a
259 subpopulation of the vesicles labeled by Rab5-eGFP. Early endosome force traces
260 demonstrated the expected bidirectional motility biased inwards (Fig. 3B). We predicted
261 kinesins would specifically be activated, or dyneins inactivated to generate the directional
262 bias we observed for early endosomes (Fig. 2I). Unexpectedly, the stall force distributions
263 for early endosomes shifted towards higher forces in both outward and inward directions
264 with S421Dhtt (Fig. 3C), suggesting both kinesins and dyneins were activated. In cells,
265 each kinesin motor exerts forces of 2-7 pN, and each dynein exerts approximately 2-3 pN
266 (Blehm et al., 2013). Looking closely at the distributions, we observe frequent kinesin
267 forces around 3 pN and 6 pN for cells with WThtt (Fig. 3C). Both of those populations are
268 observed in S421Dhtt cells, in addition to high force events near 9 pN and 12 pN.
269 Observing the inward directed forces, WT cells show frequent dynein forces near 1.5 pN
270 and 5 pN, while forces shift to ~ 3.5 pN, 9 pN, and 13 pN in S421Dhtt cells. Together,
271 these forces likely correspond to ~1-2 active kinesins and 1-3 active dyneins in WT cells,
272 and 1-4 active kinesins and 2-6 active dyneins in S421D cells, which is slightly lower than
273 previous estimates for late phagosomes (Chaudhary et al., 2018; Hendricks et al., 2010).
274 We then sought to determine how the force-dependent unbinding rates of each motor
275 were affected by S421Dhtt, predicting that the kinesin motors would have slower
276 unbinding and therefore induce the kinesin-based directional bias (Fig. 2I). The unbinding
277 rates of kinesin and dynein teams on early phagosomes in WT cells is similar (Fig. 3D,

278 Table S1). We observed slower unbinding under load of both kinesin and dynein teams
279 with S421Dhtt, consistent with more kinesin and dynein motors engaged with the
280 microtubule (Fig. 3D, Table S1). Next, we measured the binding rate of early endosomes
281 moving inwards and outwards and found the binding rate for early endosomes was
282 increased for both directions in S421Dhtt cells (Fig. 3G, H). The binding rate was more
283 strongly enhanced for outward forces, suggesting an increased number of active kinesins
284 enhances binding compared to WThtt (Fig. 3G). Observing the cumulative distribution
285 functions, we note that outward and inward motor binding rates in S421Dhtt cells were
286 very similar (Fig. 3H). This suggests that the kinesins are being activated to the same
287 level as the dyneins, reducing the native inward bias for these cargoes. In summary, the
288 force data indicate that huntingtin phosphorylation at site S421 increases the net force
289 generation, affinity, and binding strength of both kinesin and dynein motors in early
290 endosomes.
291
292 **S421Dhtt increases lysosome microtubule binding and resistance to unbinding**
293 **under load**
294
295 Like for early endosomes, we hypothesized that kinesins would have increased activity
296 on lysosomes as they also demonstrated an increased run length and outward directional
297 bias (Fig. 2H, J). We measured the force characteristics of phagolysosomes by modifying
298 the optical tweezers assay described for early endosomes with a longer incubation time
299 of 1-2 hrs. The phagolysosomes measured in the optical tweezer experiments, termed
300 lysosomes hereafter, represent a subpopulation of lysotracker-positive lysosomes,
301 compared to our earlier analysis tracking all lysotracker-positive vesicles (Fig. 2). Sample
302 force traces demonstrated typical bidirectional motility of lysosomes (Fig. 3B). We
303 observed an increase in forces in both directions for lysosomes as for the early
304 endosomes, although to a lesser degree (Fig. 3E). The balance of kinesin to dynein forces
305 remained similar in both control and S421Dhtt conditions, as expected for these
306 bidirectional cargoes. Predicting the number of motors as described for early endosomes,
307 the force distributions suggest that 1-2 additional kinesins and 1-2 additional dyneins are
308 engaged in S421Dhtt cells. The unbinding rates indicate that kinesin teams are more

309 resistant to unbinding than dyneins for lysosomes (Fig. 3F). In S421Dhtt cells, we
310 observed a slightly lower resistance to unbinding for lysosomes moving outward, while
311 the unbinding resistance was higher than WT for inward-moving cargoes (Fig. 3F, Table
312 S1). Finally, we examined the binding rates for lysosome motors to determine how
313 S421Dhtt affected microtubule affinity. S421Dhtt increased the binding rate for both
314 inward- and outward- directed cargoes compared to WT (Fig. 3I, J). The increased forces
315 and enhanced binding we observed in S421Dhtt cells suggests htt phosphorylation
316 recruits and/or activates both kinesins and dyneins.
317
318 **S421Dhtt increases kinesin and dynein association to microtubules**
319
320 As we did not observe increased kinesin activity compared to dynein upon S421
321 phosphorylation, we asked if more kinesins were engaged with microtubules to generate
322 the observed directional bias. We used immunofluorescence imaging to approximate the
323 differences in the number of motors associated with microtubules in each cell type. We
324 fixed the cells with methanol to remove cytosolic components and determine the relative
325 number of motors that were bound to microtubules in each condition at the time of fixation
326 (Fig. 4A, B). We then created intensity heatmaps of all images from the microtubules and
327 kinesin-1 heavy chain (KHC) or dynein intermediate chain (DIC) and plotted them on the
328 same axes (Fig. 4C-F). We detected higher intensities in the motors channel for both KHC
329 and DIC in the S421Dhtt cells (Fig. 4C-F). The higher intensity indicates a higher
330 concentration of motors on extracted microtubules in the S421Dhtt cells. Upon calculating
331 the correlation coefficients between the microtubule and motor channels for each
332 individual image, we observed that the dynein and microtubule intensities were more
333 highly correlated in S421Dhtt cells than WT cells. This assay demonstrates that S421Dhtt
334 increases the fraction of kinesin and dynein motors associated to microtubules. This
335 supports our data from the optical tweezers analysis, which showed a higher binding rate
336 and lower unbinding rate for motors in the S421Dhtt cells in both early endosomes and
337 lysosomes. Further, the signal for microtubule-bound kinesin and dynein motors is higher
338 in S421Dhtt cells, suggesting htt S421 phosphorylation increases the engagement of both
339 kinesins and dyneins with microtubules.

340

341 **DISCUSSION**

342

343 Our results show that huntingtin phosphorylation at S421 increases the number of active
344 kinesin and dynein motors on endosomes. Surprisingly, huntingtin activates microtubule
345 motors on endosomes at varying stages of maturation, from early endosomes to
346 lysosomes. Huntingtin also regulates the motility of neuronal signalling vesicles including
347 BDNF (Colin et al., 2008; Zala et al., 2008). In contrast, most cargo adaptors are recruited
348 to specific cargoes at specific stages of maturation (Cason et al., 2021; Mogre et al.,
349 2021). The ubiquitous function of huntingtin on a wide array of cargoes illustrates its role
350 as a central regulator of vesicular transport.

351

352 While kinesin and dynein teams exert more force and have enhanced microtubule binding
353 on both early endosomes and lysosomes in S421D huntingtin cells (Fig. 3,4), its effect on
354 the motility of different endocytic cargoes varies. For early endosomes, huntingtin
355 phosphorylation results in a pronounced shift in motility from primarily inward towards the
356 cell center to bidirectional motility (Fig. 2I). The processivity and displacement of early
357 endosomes are only weakly affected (Fig. 2E, F). In comparison, lysosomes display a
358 small but significant shift in motility towards the cell periphery in phosphomimetic htt cells
359 compared to control cells (Fig. 2J) while their run length is strongly enhanced (Fig. 2H).
360 Taken together, these results suggest that huntingtin phosphorylation regulates transport
361 by enhancing the activity of both kinesin and dynein (Fig. 5A, B). However, its effects on
362 the motility of different cargoes depend on their basal motility characteristics. In the basal
363 condition, early endosome motility is strongly biased towards the cell center. Activating
364 both kinesin and dynein results in a loss of the inward bias. Lysosome motility is
365 approximately equally distributed towards the cell center and periphery, such that
366 activating kinesin and dynein does not alter directionality, but rather increases the total
367 run length.

368

369 Disrupting actin filaments resulted in an increased outward motility similar to the effect of
370 S421Dhtt (Fig. S1A-D), suggesting a potential role for myosin VI-mediated tethering to

371 actin filaments (Sahlender et al., 2005) in generating the directional bias (Al-Haddad et
372 al., 2001). Yet, optical trapping and immunofluorescence show that S421Dhtt results in
373 enhanced forces and recruitment to microtubules for both kinesin and dynein (Figs. 3, 4),
374 suggesting S421D phosphorylation instead acts through activating microtubule motors.
375 Thus, we hypothesize that outward directional bias occurs in situations where microtubule
376 motors dominate transport. That could be achieved either by reducing tethering on actin
377 or by engaging more kinesins and dyneins.
378
379 Our findings are in broad agreement with previous studies showing that overexpressing
380 S421Dhtt resulted in increased outward motility of BDNF and TI-VAMP vesicles
381 compared to cells expressing phosphoresistive S421A htt constructs (Colin et al., 2008;
382 Zala et al., 2008). Further, Colin et al. observed increased kinesin-1 recruitment to
383 microtubules and enhanced interactions between the p150glued subunit of dynactin and
384 KHC upon S421Dhtt expression (Colin et al., 2008). Interestingly, we did not see KHC-
385 specific recruitment to microtubules with endogenous S421Dhtt compared to wild-type.
386 Instead, we observed an increase in recruitment of both motors, with slightly higher
387 dynein recruitment. These differences between previous results and our observations
388 may reflect effects of htt overexpression. Alternatively, they may be due to differences in
389 htt function in the embryonic kidney cells used here compared to previous studies in
390 neurons, which are highly polarized and have higher endogenous htt expression.
391
392 Overexpression of htt alters the processivity, run length, and directional bias of early
393 endosomes and lysosomes. The effects of overexpression are highly variable and often
394 do not reflect the trends observed when inducing mutations in the endogenous htt (Fig.
395 2), suggesting that maintaining the stoichiometry of htt to its many interacting proteins is
396 critical. We expect that excess htt in the cytoplasm is interacting with and sequestering
397 the motors and adaptors required to generate the effect that we observe in transport upon
398 overexpression (Fig. 5C). This result supports the known consequences of
399 overexpression experiments, which cause adverse effects by changing the stoichiometry
400 of interactions with other proteins in the cell. For example, overexpressing the p50
401 dynamitin subunit of dynactin causes a dominant negative effect in which early

402 endosomes and lysosomes become peripherally localized due to dynein sequestration
403 (Burkhardt et al., 1997). Regardless of the phosphorylation state, overexpression of htt
404 affected the directional bias of early endosomes and lysosomes. Processivity and run
405 lengths were increased for lysosomes in cells overexpressing either WT or S421Dhtt,
406 however, early endosomes only demonstrated this effect overexpressing S421Dhtt. This
407 work, supported by many previous studies discussing expression levels (e.g. (Burkhardt
408 et al., 1997; Dambournet et al., 2018)) highlights the importance of examining protein
409 function at endogenous expression levels to ensure biological relevance of the effects.
410 This is particularly important for scaffolding proteins like huntingtin, which mediates
411 interactions among many adaptors, effectors, motors, and membranes.
412
413 Transport is tightly regulated on multiple levels within the cell to ensure specific cargoes
414 arrive at their intracellular destination. Scaffolding proteins such as htt are a primary
415 mechanism of regulation that mediate interactions between cargoes and motor proteins,
416 and are the only known level of regulation that is cargo specific (Cason et al., 2021; Colin
417 et al., 2008; Fu and Holzbaur, 2014). Many scaffolds specifically interact with a limited
418 set of cargoes and are regulated by post-translational modifications (Cason et al., 2021;
419 Fu and Holzbaur, 2013; Fu and Holzbaur, 2014; Reed et al., 2006; Sun et al., 2017).
420 Here, we illustrate the role of htt in regulating early endosome and lysosome transport.
421 Htt S421 phosphorylation activates kinesin and dynein on both early endosomes and
422 lysosomes. However, enhanced kinesin and dynein activity differentially affects early
423 endosomes and lysosomes, influencing their direction, motor activity, and affinity for
424 microtubules. Our results underscore the central role of huntingtin in directing endosome
425 transport and suggest that huntingtin mutations likely result in cargo-specific disruptions
426 to both signalling and degradative pathways.
427
428 **MATERIALS AND METHODS**
429
430 **Cell Culture**
431 We passaged HEK293T cells (donated by Dr. Kamen's lab) at 80% or higher confluency
432 in a biosafety cabinet starting by rinsing with 2.5 mL 37 °C 1X phosphate buffered saline
433 (PBS, Wisent, St-Jean-Baptiste, QC, Canada), followed by adding 400 µL of 4 °C 0.25%

434 trypsin (Wisent) and incubating for 5 mins at 37 °C. Next, we used 5 mL of 37 °C complete
435 medium (Dulbecco's Modified Eagle Medium (DMEM), 10% fetal bovine serum (FBS), 2
436 mM Glutamax, 60 µg/mL penicillin 100 µg/mL streptomycin, all components from Gibco,
437 Waltham, MA, United States) to neutralize the trypsin activity. Finally, we placed a 1/5-
438 1/20 dilution of the resuspended cells in 37 °C fresh complete medium and transferred to
439 the 37 °C, 5% CO_2 incubator. We tested all stocks of cells for mycoplasma.
440
441 **CRISPR Design and Molecular cloning**
442 We transfected HEK293T cells with 1.25 µg of lentiCRISPR v2 cassette and 1.25 µg of
443 the single-stranded oligodeoxynucleotice (ssODN) for 24-36 hrs. lentiCRISPR v2 was a
444 gift from Feng Zhang (Addgene plasmid # 52961 ; http://n2t.net/addgene:52961 ;
445 RRID:Addgene_52961, Watertown, MA, United States) (Sanjana et al., 2014).
446 Subsequently, we selected expressing cells using 2 µg puromycin for 48-72 hrs. Finally,
447 we isolated single cells using fluorescence activated single cell sorting and grew them for
448 2-3 weeks in complete media containing 50% FBS. We verified clones containing the
449 S421D sequence with next-generation sequencing.
450
451 gRNA sequence:
452 GTTCCACAATACTCCCACTACGG
453 ssODN sequence:
454 ACGCCTCCACCCGAGCTTCTGCAAACCCTGACCGCAGTCGGGGGCATTGGGCAG
455 CTCACCGCTGCTAAGGAGGAGTCTGGTGGCCGATCTCGTAGTGGGGATATTGTGG
456 AACTTATAGGCAAGTTATTAGCAAGGTCTACTCTTACAATTAACTTTGCAGTAATAC
457 TAGTTACACTCTATTGATTATGGGCCTGCCCTGT
458 Sequencing primers:
459 Forward: CACCGTTCCACAATACTCCCACTA
460 Reverse: AAACTAGTGGGAGTATTGTGGAAC
461
462 **Plasmids and Transfection**
463 We transfected cells with 0.8 µg of eGFP-Rab5 or mCherry-S421D-htt or mCherry-WT-
464 htt huntingtin constructs 24-48 hrs before imaging. mCherry-S421D-htt and mCherry-WT-

465 htt constructs were generously donated from the Saudou lab, generated from the full
466 length pARIS-htt (Pardo et al., 2010) using methods from their previous work (Humbert
467 et al., 2002). We replaced cell culture medium in the 35 mm round glass bottom dishes
468 (Mattek, Ashland, MA, United States) containing the cells with 0.2 mL serum-free DMEM.
469 In separate 1.5 mL tubes, we added 2 µL/dish Lipofectamine 2000 (ThermoFisher
470 Scientific, Waltham, MA, United States) to 50 µL/dish serum-free DMEM and added 0.8
471 µg/dish of DNA to 50 µL/dish of serum-free DMEM. We then mixed the DNA and
472 lipofectamine, incubated for 20 mins at room temperature, and added 100 µL/dish to the
473 cells. Four hours later, we replaced the serum-free medium with complete media.
474
475 **Western Blotting**
476 We lysed cells by manually twisting while lifting and descending a Dounce homogenizer
477 20-30 times in 400 µL PBS containing 0.01 M dithiothreitol (DTT, R0681, ThermoFisher
478 Scientific) and 1X protease inhibitor cocktail (100X stock from PIC002, Bioshop,
479 Burlington, ON, Canada) on ice. Subsequently, we centrifuged the cell solution at 1500 g
480 for 10 mins at 4 °C, then centrifuged the supernatant at 16000 g for 10 mins at 4 °C. We
481 added 20 µL of lysate for each sample to the SDS-PAGE gel, diluted in 2x Laemmli buffer
482 (161-0737, Biorad, Hercules, CA, USA) with 2.5% 2-mercaptoethanol (M6250, Sigma,
483 Burlington, MA, United States) after heating to 100 °C for at least 10 mins. To mark
484 molecular weights, we loaded 5 µL of protein ladder (PI26634, ThermoFisher Scientific).
485 We used a 25 mM Tris (TRS001.1, Bioshop), 190 mM glycine (800-045-LG, Wisent), and
486 0.1% SDS (SDS999.100, Bioshop) running buffer, and ran the gel at 80 mA for 60-90
487 mins. To transfer, we used 25 mM Tris, 190 mM glycine, and 30% methanol (34860-4L-
488 R, Sigma) transfer buffer for wet transfer at 100 V for 90 mins with a PVDF membrane.
489 We blocked the membrane for 1 hour with blocking buffer: 5% bovine serum albumin
490 (BSA, Bioshop) in tris-buffered saline with Tween 20 (TBST, 20 mM Tris, 150 mM NaCl
491 (SOD004.1, Bioshop), 0.1% Tween 20 (P2287, Sigma). We diluted primary antibodies in
492 the blocking buffer and incubated at 4 °C overnight. Next, we washed the membrane with
493 blocking buffer 3 times for 5 mins and incubated with the secondary antibody diluted in
494 blocking buffer for 90 mins with constant agitation. We washed the membrane 3 times
495 with TBST before incubating with a 1:1 ratio of horseradish peroxidase substrate and

496 enzyme mixture (P90720, EMD Millipore, Burlington, MA, USA). We imaged using a
497 Biorad Chemidoc camera set to detect chemiluminescence. We subsequently stained the
498 membrane with Coomassie G-250 (CBB555.25, Bioshop), using a previously established
499 protocol from Goldman et al. titled Coomassie blue R-250 staining (Goldman et al., 2016).
500 We used the following primary antibodies: 1/1000 dilution of T9026 ms α-tubulin, Sigma
501 lot: 000089497, and 1/500 dilution of MAB2166 ms-huntingtin, Abcam, Cambridge,
502 England lot: 3703568. The secondary antibody was rabbit anti-mouse ab6728, Abcam.
503
504 **Motility Assay**
505 In a biological safety cabinet, we mixed 200 µL of 37 °C complete medium with
506 LysoTracker™ Deep Red (L12492, ThermoFisher Scientific) to a concentration of 70 nM
507 and added it to HEK293T cells in MatTek 35 mm glass bottom dishes. Cells were
508 incubated for 10 mins at 37 °C, and subsequently replaced the medium with 1 mL of 37
509 °C Lebovitz (11415064, Gibco) with 10 % FBS for imaging. We imaged cells in a 37°C
510 chamber of a Nikon Eclipse Ti-E microscope in near-total internal reflection (TIRF)
511 fluorescence settings using an EMCCD camera with an exposure time of 120 ms for 3
512 mins. We repeated the process for several cells within each dish and all cells were imaged
513 within 1 hour of adding the Lysotracker. For Rab5 transfected cells, we replaced the
514 medium with 0.5-1 mL of of 37 °C Lebovitz with 10 % FBS and imaged them as the
515 lysosomes. For experiments using 250 nM latrunculin A (S428021, Sigma) or 10 µM
516 nocodazole (M1404, Sigma), we added the drug to the Lebovitz medium a minimum of
517 15 mins prior to imaging.
518
519 **Immunofluorescence: Cytoskeleton and Golgi Apparatus**
520 This protocol was adapted from Jimenez et al. (Jimenez et al., 2020). We passaged
521 HEK293T cells onto rectangular coverslips (12544-A ThermoFisher Scientific) in 100 mm
522 petri dishes (83.3902, Sarstedt, Saint-Leonard, QC, Canada) ~24 hrs prior to fixation. We
523 performed incubations for extraction, fixing and $NaBH_4$ (452882, Sigma) solutions on flat
524 pieces of parafilm, with droplets containing 100 µL of the described solution. Using fine-
525 tipped tweezers, we manipulated the coverslips and placed them cell-side down on the
526 droplets. Firstly, we incubated the cell-adhered coverslips with 37 °C extraction solution

527 (0.25% Triton-X-100 (X100, Sigma), 0.1% glutaraldehyde (G5882, Sigma)) in PEM
528 (80mM PIPES (P6757, Sigma), 5mM EGTA (EGT101, Bioshop), 2mM $MgCl_2$ (M2866,
529 Sigma) at pH=6.8) for 15-45 s. We next fixed the cells with 37 °C 0.25% Triton-X-100 and
530 0.5% glutaraldehyde in PEM and incubated for 10 mins. We subsequently transferred the
531 coverslips to 0.1% $NaBH_4$ in PBS (Wisent) and incubated for 7 mins, then rinsed quickly
532 with PBS twice before blocking. Next, we incubated the fixed cells with blocking buffer
533 (2% BSA (ALB001, Bioshop) in PBS, (Wisent)) inside a glass petri dish for 30 mins with
534 gentle rocking on an orbital shaker. Subsequently, we added a 1:400 solution of primary
535 antibody in blocking buffer (anti-GM130 ab52649 Abcam, anti-tubulin Sigma T6199) in
536 100 µL droplets on a parafilm-coated humid chamber. We incubated coverslips with the
537 primary antibody droplets overnight at 4 °C. We then performed 3x 10-minute washes
538 with ~10 mL blocking buffer in glass petri dishes. After washing, we added a 1:400 dilution
539 of fluorescent secondary antibody, goat anti-mouse 594 (A11032, ThermoFisher) and
540 goat anti-rabbit (18772, Sigma), to the humid chamber with new parafilm and incubated
541 it for 1 hr at room temperature protected from light. We then washed as described after
542 primary antibody incubation. To label actin, we added phalloidin (P1951, Sigma) labeled
543 with Alexa-647 (0.094 µM in PBS) and incubated for 20 mins on 100 µL droplets in the
544 humid chamber. We transferred coverslips to PBS, then set up for imaging by sealing
545 them to a glass slide with double sided tape and vacuum grease to a glass slide and
546 adding PBS to the channel. Finally, we imaged the cells in ~1.5-2 µm thick z-stacks using
547 near-TIRF microscopy, with 1 mW laser power at 640 nm, 561 nm, and 488 nm excitation,
548 600 ms exposure time, EM gain of 200 using an EMCCD camera of a Nikon Eclipse Ti-E
549 microscope.
550
551 **Immunofluorescence: Motor Colocalization**
552 This protocol differs from cytoskeletal imaging in the fixation step; we incubated cells at -
553 20 °C with 1 mM EGTA (EGT101, Bioshop) in -20 °C methanol, for 8 mins. Subsequent
554 steps are identical to the cytoskeletal immunofluorescence protocol, except that the
555 blocking buffer contained 0.2% saponin (4521, Sigma). We first imaged cells for the motor
556 (kinesin or dynein) and saved their positions on the microscope. Following imaging, we
557 washed the sample and probed for tubulin while maintaining the slide in the same position

558 on the microscope, using another colour and shorter incubation times to allow higher
559 throughput. The protocol was as follows: 1 hr incubation with primary antibody, wash 3x
560 slide volume with blocking buffer, 45 mins incubation with secondary antibody, wash 3x
561 slide volume with PBS, this sequential antibody staining was done due to the redundancy
562 in antibody species available. The primary antibodies used for experiments were: 1/400
563 T9026 ms alpha-tubulin, Sigma lot: 000089497, 1/400 ms-kinesin heavy chain MAB1614
564 lot: 3593684, 1/400 MAB1618 ms-dynein, cytoplasmic lot: 3089121. Secondary
565 antibodies used for experiments were goat anti-mouse 488 (A21236, ThermoFisher) for
566 motors followed by Goat anti-mouse 647 (A21236, Sigma) for microtubules.
567
568 **Immunoflurescence: Huntingtin Localization**
569 We fixed the cells with prewarmed 4% paraformaldehyde at 37 °C for 10 mins, and
570 subsequently followed the protocol as outlined for cytoskeletal imaging. The huntingtin
571 antibody used was MAB2166 ms-huntingtin, Abcam lot: 3703568.The blocking buffer
572 contained 0.2% saponin (4521, Sigma).
573
574 **Immunofluorescence: Mitochondria**
575 We fixed cells using prewarmed 4% paraformaldehyde at 37 °C for 20 mins, followed by
576 3 washes with PBS. Using 50 mM NH_4Cl in PBS, we quenched fixation for 10 mins, and
577 washed again 3 times with PBS. We permeabilized cells using 0.1% TritonX-100 in PBS
578 for 10 mins with gentle rocking, followed by blocking with 10% BSA (ALB001, Bioshop)
579 for 30-45 mins with gentle rocking. We diluted the primary antibody 1/500 (TOMM40
580 18409-1-AP, Proteintech, Rosemont, IL, United States) with 5% BSA in PBS and
581 incubated overnight at 4 °C. We washed coverslips 3 times with gentle rocking using the
582 5% BSA in PBS. We diluted the secondary antibody 1/400 in the same solution and
583 incubated for 1 hr at room temperature. We repeated the washing described after the
584 primary antibody incubation, then mounted the slide using PBS as the imaging medium.
585 We imaged samples using an Olympus IX83 with a 100x objective using a disk scanning
586 unit to obtain high resolution z stacking in a 25 μm range using 0.5 μm slices.
587
588 **Intracellular Optical Tweezers**

589 We prepared a fibronectin (356008 Corning, Bedford, MA, United States) stock at a
590 concentration of 1.4 mg/mL in water and stored it at -20 °C until use. We coated
591 fluorescent yellow/green 500 nm beads (F8813, ThermoFisher Scientific) by centrifuging
592 20 µL of stock bead solution at 20000 rcf for 5 mins, then resuspended the beads in 25
593 µL of the fibronectin solution. We incubated the beads overnight at 4 °C, then washed
594 with 40 µL PBS 3 times, centrifuging again at 20000 rcf for 5 mins each. We diluted this
595 bead solution 1/20 in DMEM complete media, sonicated for 5 mins, and incubated with
596 the cells for 10 mins at 37 °C. For imaging, we replaced the medium with Lebovitz
597 supplemented with 10% FBS. Early endosome data was acquired from 15 mins–50 mins
598 after bead internalization, while lysosomes were from 1 - 2 hours post-internalization. We
599 identified cargoes moving processively within the cell, positioned the location of the center
600 of the optical tweezer laser above the motile cargo, and opened the shutter to capture the
601 bead. We acquired 60 s force traces holding the optical tweezer laser (12 W, 1064 nm)
602 fixed in the original capture position, while monitoring the position signal and live image
603 to ensure that the bead remained within one bead radius of the center of the tweezer.
604 Immediately after this measurement, we calibrated the optical tweezers by applying a 275
605 s multifrequency sinusoid to calculate the position sensitivity (β), trap stiffness (k_{trap}), and
606 viscoelastic properties (G', G'', Fig. S2E, F) of the cytoplasm as previously described
607 (Chaubet et al., 2020).
608
609 **Immunofluorescence Analysis: Actin, Microtubules, Golgi, Huntingtin**
610 For each z-stack, we chose the sharpest image for each channel for qualitative analysis
611 and observation as overlays.
612
613 **Mitochondrial Immunofluorescence Analysis**
614 We determined the range of z-values with samples in focus, and only used those slices
615 for image analysis. We processed the images in Fiji with the white top hat 3D
616 morphological filter, using a radius of 5 in x and y, and 2 in z. We then set an automatic
617 threshold and converted the thresholded image to a mask. Next, we ran the analyze
618 particles function to determine the shape, area, and number of mitochondria in each

plane, repeated for all in focus z planes, and added all the values for each z plane together. We plotted the results from all cells using MATLAB.

Golgi Dispersal Analysis

Using ImageJ, we observed each of the Golgi images using the same linear LUT (minimum = 145 a.u. and maximum = 1885 a.u.) and then categorized the Golgi into organized, dispersed, or undetermined. Comparing the results from multiple experiments using this binary categorization and excluding the undetermined data, we determined the percentage of organized and dispersed Golgi observed in each cell type.

Motility Assay Analysis- Tracking

We used the Fiji plugin TrackMate (Tinevez et al., 2017) to generate tracks from the images for subsequent analysis. The settings used in TrackMate highly influence the results and are therefore shown in the tables below (Table 1 and 2). We chose the parameters by comparing the maximum intensity projection of all frames with the generated tracks and trying multiple values that would be considered logical for these cargos.

Table 1. TrackMate analysis settings used in the analysis of lysosomal cargoes using LysoTracker™.

Parameter	Value
Estimated blob diameter	1 μm
Intensity threshold	400
Linking maximum distance	0.5 μm
Gap-closing maximum distance	0.5 μm
Gap-closing maximum frame gap	2

Table 2. TrackMate analysis settings used in the analysis of early endosomal cargoes using Rab5-eGFP transfected cells.

Parameter	Value
Estimated blob diameter	0.8 μm
Intensity threshold	300
Linking maximum distance	0.5 μm
Gap-closing maximum distance	0.5 μm

Motility Assay Analysis-Quantitation

To analyze the raw TrackMate data, we wrote custom MATLAB codes, now available on GitHub: https://github.com/hendricks-lab.

We calculated time averaged mean squared displacement according to the following formula:

$$MSD = \frac{1}{\tau - t}\sum_{t=0}^{\tau-t}(x_{t+1} - x_t)^2$$

We calculated α values by fitting a line to the log-log plot of the mean squared displacement for time delays from 120 ms-5 s. We obtained radius of gyration values using the following formula:

$$R_g^2 = \frac{1}{N}\sum_{k=1}^{N}(r_k - r_{mean})^2$$

Optical Tweezers: Force Trace Analysis

We calculated the trap stiffness and position sensitivity from the calibration data as previously described (Chaubet et al., 2020). Using the calibration data, we converted 60 s position traces to force traces (Fig. S2D) and calculated the viscoelastic moduli in each condition (Fig. S2B, C). We observed brightfield images of the position of the trap and the cell's nucleus to define the directionality of the cargo's movement. Any force event that had a maximum off-axis force, a force in the direction perpendicular to the defined microtubule axis, above 75% of the median on-axis forces, forces along the direction of the microtubule, were excluded. Stall forces were binned into 1 pN size bins and counted as stalls if the duration that they were above 0.5 pN duration was longer than 0.1 s. We calculated binding rates from the force traces by identifying the times that the cargoes unbound from the microtubules after a stall event and determining the time between unbinding and rebinding to the microtubule. We calculated force-dependent unbinding rates from the stall force event before a cargo became detached and categorized them

by the direction the cargo was travelling immediately prior to detachment, as previously described (Berger et al., 2019). We performed an exponential fit to the data and presented it in Table S1 following the equation below with U as the unbinding rate, U_0 as the force-independent unbinding rate, F as the force, and F_d as the detachment force.

$$\boldsymbol{U = U_0 e^{\frac{F}{F_d}}}$$

Statistical Analysis

We analysed all pairwise histogram comparisons and cumulative distribution functions using the Kolmogorov-Smirnov (ks) test. We used Student's two-tailed t-test for all pairwise analyses of violin plots. For optical tweezers stall force distribution analyses, in addition to the ks test we performed bootstrapping. We took 1000 bootstrap means of samples equivalent to the number of datapoints for the condition being tested. We then calculated 95% confidence intervals from the bootstrap mean distribution using the quantile function in MATLAB. To calculate p-values for bootstrap samples (not reported in Fig. 3), we subtracted the control from the S421D condition for each of the 1000 bootstrap means for the conditions to be compared and plotted the distribution (Fig. S2E). The p-value was determined by the fraction of data that overlapped with the 0 value, if this fraction was lower than 0.05, the difference between the values was considered statistically significant.

ACKNOWLEDGEMENTS

We thank Frederic Saudou (U. Grenoble) for generously sharing huntingtin constructs, Amine Kamen (McGill U.) for guidance on CRISPR/Cas9, and the members of the Hendricks lab for thoughtful comments on the manuscript.

COMPETING INTERESTS

The authors report no competing interests.

FUNDING

ENPP is supported by a CGS-M fellowship from the Natural Sciences and Engineering Council of Canada. AGH is supported by the Canadian Institutes for Health Research (PJT-159490).

700 **REFERENCES**

701

702 **Al-Haddad, A., Shonn, M. A., Redlich, B., Blocker, A., Burkhardt, J. K., Yu, H.,**
703 **Hammer, J. A., Weiss, D. G., Steffen, W., Griffiths, G., et al.** (2001). Myosin Va
704 bound to phagosomes binds to F-actin and delays microtubule-dependent motility.
705 *Mol. Biol. Cell* **12**, 2742–2755.

706 **Bentley, M., Decker, H., Luisi, J. and Banker, G.** (2015). A novel assay reveals
707 preferential binding between rabs, kinesins, and specific endosomal
708 subpopulations. *J. Cell Biol.* **208**, 273–281.

709 **Berger, F., Klumpp, S. and Lipowsky, R.** (2019). Force-Dependent Unbinding Rate of
710 Molecular Motors from Stationary Optical Trap Data. *Nano Lett.* **19**, 2598–2602.

711 **Blehm, B. H., Schroer, T. A., Trybus, K. M., Chemla, Y. R. and Selvin, P. R.** (2013).
712 In vivo optical trapping indicates kinesin's stall force is reduced by dynein during
713 intracellular transport. *Proc. Natl. Acad. Sci. U. S. A.* **110**, 3381–3386.

714 **Blocker, A., Severin, F. F., Burkhardt, J. K., Bingham, J. B., Yu, H., Olivo, J. C.,**
715 **Schroer, T. A., Hyman, A. A. and Griffiths, G.** (1997). Molecular requirements for
716 bi-directional movement of phagosomes along microtubules. *J. Cell Biol.* **137**, 113–
717 129.

718 **Burkhardt, J. K., Echeverri, C. J., Nilsson, T. and Vallee, R. B.** (1997).
719 Overexpression of the dynamitin (p50) subunit of the dynactin complex disrupts
720 dynein-dependent maintenance of membrane organelle distribution. *J. Cell Biol.*

721 **Cason, S. E., Carman, P., Van Duyne, C., Goldsmith, J., Dominguez, R. and**
722 **Holzbaur, E. L. F.** (2021). Dynein effectors regulate autophagosome motility
723 Sequential dynein effectors regulate axonal autophagosome motility in a
724 maturation-dependent pathway. *J. Chem. Biol.*

725 **Caviston, J. P. and Holzbaur, E. L. F.** (2009). Huntingtin as an essential integrator of
726 intracellular vesicular trafficking. *Trends Cell Biol.*

727 **Caviston, J. P., Ross, J. L., Antony, S. M., Tokito, M. and Holzbaur, E. L. F.** (2007).
728 Huntingtin facilitates dynein/dynactin-mediated vesicle transport. *Proc. Natl. Acad.*
729 *Sci. U. S. A.* **104**, 10045–10050.

730 **Caviston, J. P., Zajac, A. L., Tokito, M. and Holzbaur, E. L. F.** (2011). Huntingtin

731 coordinates the dynein-mediated dynamic positioning of endosomes and
732 lysosomes. *Mol. Biol. Cell*.
733 **Chaubet, L., Chaudhary, A. R., Heris, H. K., Ehrlicher, A. J. and Hendricks, A. G.**
734 (2020). Dynamic actin cross-linking governs the cytoplasm's transition to fluid-like
735 behavior. *Mol. Biol. Cell* **31**, 1744–1752.
736 **Chaudhary, A. R., Berger, F., Berger, C. L. and Hendricks, A. G.** (2018). Tau directs
737 intracellular trafficking by regulating the forces exerted by kinesin and dynein
738 teams. *Traffic* **19**, 111–121.
739 **Chung, P. J., Song, C., Deek, J., Miller, H. P., Li, Y., Choi, M. C., Wilson, L.,**
740 **Feinstein, S. C. and Safinya, C. R.** (2016). Tau mediates microtubule bundle
741 architectures mimicking fascicles of microtubules found in the axon initial segment.
742 *Nat. Commun.* **7**, 1–9.
743 **Colin, E., Zala, D., Liot, G., Rangone, H., Borrell-Pagès, M., Li, X. J., Saudou, F.**
744 **and Humbert, S.** (2008). Huntingtin phosphorylation acts as a molecular switch for
745 anterograde/retrograde transport in neurons. *EMBO J.*
746 **Corthésy-Theulaz, I., Pauloin, A. and Pfeffer, S. R.** (1992). Cytoplasmic dynein
747 participates in the centrosomal localization of the Golgi complex. *J. Cell Biol.* **118**,
748 1333–1345.
749 **Dambournet, D., Sochacki, K. A., Cheng, A. T., Akamatsu, M., Taraska, J. W.,**
750 **Hockemeyer, D. and Drubin, D. G.** (2018). Genome-edited human stem cells
751 expressing fluorescently labeled endocytic markers allow quantitative analysis of
752 clathrin-mediated endocytosis during differentiation. *J. Cell Biol.* **217**, 3301–3311.
753 **Davies, S. W., Turmaine, M., Cozens, B. A., DiFiglia, M., Sharp, A. H., Ross, C. A.,**
754 **Scherzinger, E., Wanker, E. E., Mangiarini, L. and Bates, G. P.** (1997).
755 Formation of neuronal intranuclear inclusions underlies the neurological dysfunction
756 in mice transgenic for the HD mutation. *Cell*.
757 **Dunah, A. W., Jeong, H., Griffin, A., Kim, Y. M., Standaert, D. G., Hersch, S. M.,**
758 **Mouradian, M. M., Young, A. B., Tanese, N. and Krainc, D.** (2002). Sp1 and
759 TAFII130 transcriptional activity disrupted in early Huntington's disease. *Science*
760 *(80-.).* **296**, 2238–2243.
761 **Duyao, M. P., Auerbach, A. B., Ryan, A., Persichetti, F., Barnes, G. T., McNeil, S.**

762 **M., Ge, P., Vonsattel, J. P., Gusella, J. F., Joyner, A. L., et al.** (1995).
763 Inactivation of the mouse huntington's disease gene homolog Hdh. *Science (80-.).*
764 **269**, 407–410.
765 **Ebneth, A., Godemann, R., Stamer, K., Illenberger, S., Trinczek, B., Mandelkow, E.**
766 **M. and Mandelkow, E.** (1998). Overexpression of tau protein inhibits kinesin-
767 dependent trafficking of vesicles, mitochondria, and endoplasmic reticulum:
768 Implications for Alzheimer's disease. *J. Cell Biol.* **143**, 777–794.
769 **Encalada, S. E., Szpankowski, L., Xia, C. H. and Goldstein, L. S. B.** (2011). Stable
770 kinesin and dynein assemblies drive the axonal transport of mammalian prion
771 protein vesicles. *Cell* **144**, 551–565.
772 **Engelender, S.** (1997). Huntingtin-associated protein 1 (HAP1) interacts with the
773 p150Glued subunit of dynactin. *Hum. Mol. Genet.*
774 **Fu, M. M. and Holzbaur, E. L. F.** (2013). JIP1 regulates the directionality of APP axonal
775 transport by coordinating kinesin and dynein motors. *J. Cell Biol.*
776 **Fu, M. meng and Holzbaur, E. L. F.** (2014). Integrated regulation of motor-driven
777 organelle transport by scaffolding proteins. *Trends Cell Biol.*
778 **Futter, M., Diekmann, H., Schoenmakers, E., Sadiq, O., Chatterjee, K. and**
779 **Rubinsztein, D. C.** (2009). Wild-type but not mutant huntingtin modulates the
780 transcriptional activity of liver X receptors. *J. Med. Genet.* **46**, 438–446.
781 **Gauthier, L. R., Charrin, B. C., Borrell-Pagès, M., Dompierre, J. P., Rangone, H.,**
782 **Cordelières, F. P., De Mey, J., MacDonald, M. E., Leßmann, V., Humbert, S., et**
783 **al.** (2004). Huntingtin controls neurotrophic support and survival of neurons by
784 enhancing BDNF vesicular transport along microtubules. *Cell* **118**, 127–138.
785 **Gil, J. M. and Rego, A. C.** (2008). Mechanisms of neurodegeneration in Huntington's
786 disease. *Eur. J. Neurosci.*
787 **Goldman, A., Harper, S. and Speicher, D. W.** (2016). Detection of proteins on blot
788 membranes - Current Protocols in Protein Science. *Curr. Protoc. Protein Sci.* 1–6.
789 **Guo, Q., Huang, B., Cheng, J., Seefelder, M., Engler, T., Pfeifer, G., Oeckl, P., Otto,**
790 **M., Moser, F., Maurer, M., et al.** (2018). The cryo-electron microscopy structure of
791 huntingtin. **555**, 117–120.
792 **Hendricks, A. G., Perlson, E., Ross, J. L., Schroeder, H. W., Tokito, M. and**

Holzbaur, E. L. F. (2010). Motor Coordination via a Tug-of-War Mechanism Drives Bidirectional Vesicle Transport. *Curr. Biol.*

Hilditch-Maguire, P. (2000). Huntingtin: an iron-regulated protein essential for normal nuclear and perinuclear organelles. *Hum. Mol. Genet.*

Holbert, S., Denghien, I., Kiechle, T., Rosenblatt, A., Wellington, C., Hayden, M. R., Margolis, R. L., Ross, C. A., Dausset, J., Ferrante, R. J., et al. (2001). The Gln-Ala repeat transcriptional activator CA150 interacts with huntingtin: Neuropathologic and genetic evidence for a role in Huntington's disease pathogenesis. *Proc. Natl. Acad. Sci. U. S. A.* **98**, 1811–1816.

Humbert, S., Bryson, E. A., Cordelières, F. P., Connors, N. C., Datta, S. R., Finkbeiner, S., Greenberg, M. E. and Saudou, F. (2002). The IGF-1/Akt pathway is neuroprotective in Huntington's disease and involves huntingtin phosphorylation by Akt. *Dev. Cell*.

Jimenez, A., Friedl, K. and Leterrier, C. (2020). About samples, giving examples: Optimized Single Molecule Localization Microscopy. *Methods*.

Leavitt, B. R., Van Raamsdonk, J. M., Shehadeh, J., Fernandes, H., Murphy, Z., Graham, R. K., Wellington, C. L., Raymond, L. A. and Hayden, M. R. (2006). Wild-type huntingtin protects neurons from excitotoxicity. *J. Neurochem.* **96**, 1121–1129.

Lemarié, F. L., Caron, N. S., Sanders, S. S., Schmidt, M. E., Nguyen, Y. T. N., Ko, S., Xu, X., Pouladi, M. A., Martin, D. D. O. and Hayden, M. R. (2021). Rescue of aberrant huntingtin palmitoylation ameliorates mutant huntingtin-induced toxicity. *Neurobiol. Dis.* **158**,.

Li, S. H., Schilling, G., Young, W. S., Li, X., Margolis, R. L., Stine, O. C., Wagster, M. V., Abbott, M. H., Franz, M. L., Ranen, N. G., et al. (1993). Huntington's disease gene (IT15) is widely expressed in human and rat tissues. *Neuron* **11**, 985–993.

Li, S. H., Gutekunst, C. A., Hersch, S. M. and Li, X. J. (1998). Interaction of Huntingtin-associated protein with dynactin P150(Glued). *J. Neurosci.*

Li, S.-H., Cheng, A. L., Zhou, H., Lam, S., Rao, M., Li, H. and Li, X.-J. (2002). Interaction of Huntington Disease Protein with Transcriptional Activator Sp1. *Mol.*

824 *Cell. Biol.* **22**, 1277–1287.
825 **Liot, G., Zala, D., Pla, P., Mottet, G., Piel, M. and Saudou, F.** (2013). Mutant
826 huntingtin alters retrograde transport of TrkB receptors in striatal dendrites. *J.*
827 *Neurosci.* **33**, 6298–6309.
828 **Lo Sardo, V., Zuccato, C., Gaudenzi, G., Vitali, B., Ramos, C., Tartari, M., Myre, M.**
829 **A., Walker, J. A., Pistocchi, A., Conti, L., et al.** (2012). An evolutionary recent
830 neuroepithelial cell adhesion function of huntingtin implicates ADAM10-Ncadherin.
831 *Nat. Neurosci.* **15**, 713–721.
832 **Marcora, E., Gowan, K. and Lee, J. E.** (2003). Stimulation of NeuroD activity by
833 huntingtin and huntingtin-associated proteins HAP1 and MLK2. *Proc. Natl. Acad.*
834 *Sci. U. S. A.* **100**, 9578–9583.
835 **McGuire, J. R., Rong, J., Li, S. H. and Li, X. J.** (2006). Interaction of Huntingtin-
836 associated protein-1 with kinesin light chain: Implications in intracellular trafficking
837 in neurons. *J. Biol. Chem.* **281**, 3552–3559.
838 **McKenney, R. J., Huynh, W., Tanenbaum, M. E., Bhabha, G. and Vale, R. D.** (2014).
839 Activation of cytoplasmic dynein motility by dynactin-cargo adapter complexes.
840 *Science (80-.).*
841 **Mogre, S. S., Christensen, J. R., Reck-Peterson, S. L. and Koslover, E. F.** (2021).
842 Optimizing microtubule arrangements for rapid cargo capture. *Biophys. J.* **120**,
843 4918–4931.
844 **Nasir, J., Floresco, S. B., O'Kusky, J. R., Diewert, V. M., Richman, J. M., Zeisler, J.,**
845 **Borowski, A., Marth, J. D., Phillips, A. G. and Hayden, M. R.** (1995). Targeted
846 disruption of the Huntington's disease gene results in embryonic lethality and
847 behavioral and morphological changes in heterozygotes. *Cell* **81**, 811–823.
848 **Pardo, R., Molina-Calavita, M., Poizat, G., Keryer, G., Humbert, S. and Saudou, F.**
849 (2010). PARIS-htt: An optimised expression platform to study huntingtin reveals
850 functional domains required for vesicular trafficking. *Mol. Brain* **3**, 1–17.
851 **Reed, N. A., Cai, D., Blasius, T. L., Jih, G. T., Meyhofer, E., Gaertig, J. and Verhey,**
852 **K. J.** (2006). Microtubule Acetylation Promotes Kinesin-1 Binding and Transport.
853 *Curr. Biol.*
854 **Sahlender, D. A., Roberts, R. C., Arden, S. D., Spudich, G., Taylor, M. J., Luzio, J.**

855 **P., Kendrick-Jones, J. and Buss, F.** (2005). Optineurin links myosin VI to the
856 Golgi complex and is involved in Golgi organization and exocytosis. *J. Cell Biol.*
857 **Sanjana, N. E., Shalem, O. and Zhang, F.** (2014). Improved vectors and genome-wide
858 libraries for CRISPR screening HHS Public Access Supplementary Material. *Nat*
859 *Methods* **11**, 783–784.
860 **Saudou, F. and Humbert, S.** (2016). The Biology of Huntingtin. *Neuron*.
861 **Schlager, M. A., Hoang, H. T., Urnavicius, L., Bullock, S. L. and Carter, A. P.**
862 (2014). In vitro reconstitution of a highly processive recombinant human dynein
863 complex . *EMBO J.* **33**, 1855–1868.
864 **Schmitt, I., Bächner, D., Megow, D., Henkiein, P., Hamelster, H., Epplen, J. T. and**
865 **Riess, O.** (1995). Expression of the huntington disease gene in rodents: Cloning
866 the rat homologue and evidence for downregulation in non-neuronal tissues during
867 development. *Hum. Mol. Genet.* **4**, 1173–1182.
868 **Sharp, A. H., Loev, S. J., Schilling, G., Li, S. H., Li, X. J., Bao, J., Wagster, M. V.,**
869 **Kotzuk, J. A., Steiner, J. P., Lo, A., et al.** (1995). Widespread expression of
870 Huntington's disease gene (IT15) protein product. *Neuron* **14**, 1065–1074.
871 **Steffan, J. S., Agrawal, N., Pallos, J., Rockabrand, E., Trotman, L. C., Slepko, N.,**
872 **Illes, K., Lukacsovich, T., Zhu, Y. Z., Cattaneo, E., et al.** (2004). SUMO
873 Modification of Huntingtin and Huntington's Disease Pathology. *Science (80-.).*
874 **304**, 100–104.
875 **Sun, T., Li, Y., Li, T., Ma, H., Guo, Y., Jiang, X., Hou, M., Huang, S. and Chen, Z.**
876 (2017). JIP1 and JIP3 cooperate to mediate TrkB anterograde axonal transport by
877 activating kinesin-1. *Cell. Mol. Life Sci.*
878 **Thion, M. S., McGuire, J. R., Sousa, C. M., Fuhrmann, L., Fitamant, J., Leboucher,**
879 **S., Vacher, S., Du Montcel, S. T., Bièche, I., Bernet, A., et al.** (2015). Unraveling
880 the Role of Huntingtin in Breast Cancer Metastasis. *J. Natl. Cancer Inst.* **107**, 1–13.
881 **Tinevez, J. Y., Perry, N., Schindelin, J., Hoopes, G. M., Reynolds, G. D., Laplantine,**
882 **E., Bednarek, S. Y., Shorte, S. L. and Eliceiri, K. W.** (2017). TrackMate: An open
883 and extensible platform for single-particle tracking. *Methods* **115**, 80–90.
884 **Twelvetrees, A. E., Yuen, E. Y., Arancibia-Carcamo, I. L., MacAskill, A. F.,**
885 **Rostaing, P., Lumb, M. J., Humbert, S., Triller, A., Saudou, F., Yan, Z., et al.**

886 (2010). Delivery of GABAARs to Synapses Is Mediated by HAP1-KIF5 and
887 Disrupted by Mutant Huntingtin. *Neuron* **65**, 53–65.
888 **Wanker, E. E., Ast, A., Schindler, F., Trepte, P. and Schnoegl, S.** (2019). The
889 pathobiology of perturbed mutant huntingtin protein–protein interactions in
890 Huntington's disease. *J. Neurochem.* **151**, 507–519.
891 **Wong, Y. C. and Holzbaur, E. L. F.** (2014). The regulation of autophagosome
892 dynamics by huntingtin and HAP1 is disrupted by expression of mutant huntingtin,
893 leading to defective cargo degradation. *J. Neurosci.*
894 **Xu, X., Ng, B., Sim, B., Radulescu, C. I., Yusof, N. A. B. M., Goh, W. I., Lin, S., Lim,**
895 **J. S. Y., Cha, Y., Kusko, R., et al.** (2020). pS421 huntingtin modulates
896 mitochondrial phenotypes and confers neuroprotection in an HD hiPSC model. *Cell*
897 *Death Dis.*
898 **Yanai, A., Huang, K., Kang, R., Singaraja, R. R., Arstikaitis, P., Gan, L., Orban, P.**
899 **C., Mullard, A., Cowan, C. M., Raymond, L. A., et al.** (2006). Palmitoylation of
900 huntingtin by HIP14is essential for its trafficking and function. *Nat. Neurosci.* **9**,
901 824–831.
902 **Zala, D., Colin, E., Rangone, H., Liot, G., Humbert, S. and Saudou, F.** (2008).
903 Phosphorylation of mutant huntingtin at S421 restores anterograde and retrograde
904 transport in neurons. *Hum. Mol. Genet.*
905 **Zeitlin, S., Liu, J., Chapman, D. L. and Papaioannou, V. E.** (1995). article nullizygous
906 for the Huntington ' s disease gene homo logue. **11**, 155–163.
907 **Zuccato, C., Tartari, M., Crotti, A., Goffredo, D., Valenza, M., Conti, L., Cataudella,**
908 **T., Leavitt, B. R., Hayden, M. R., Timmusk, T., et al.** (2003). Huntingtin interacts
909 with REST/NRSF to modulate the transcription of NRSE-controlled neuronal genes.
910 *Nat. Genet.* **35**, 76–83.
911
912

913 **FIGURE LEGENDS**

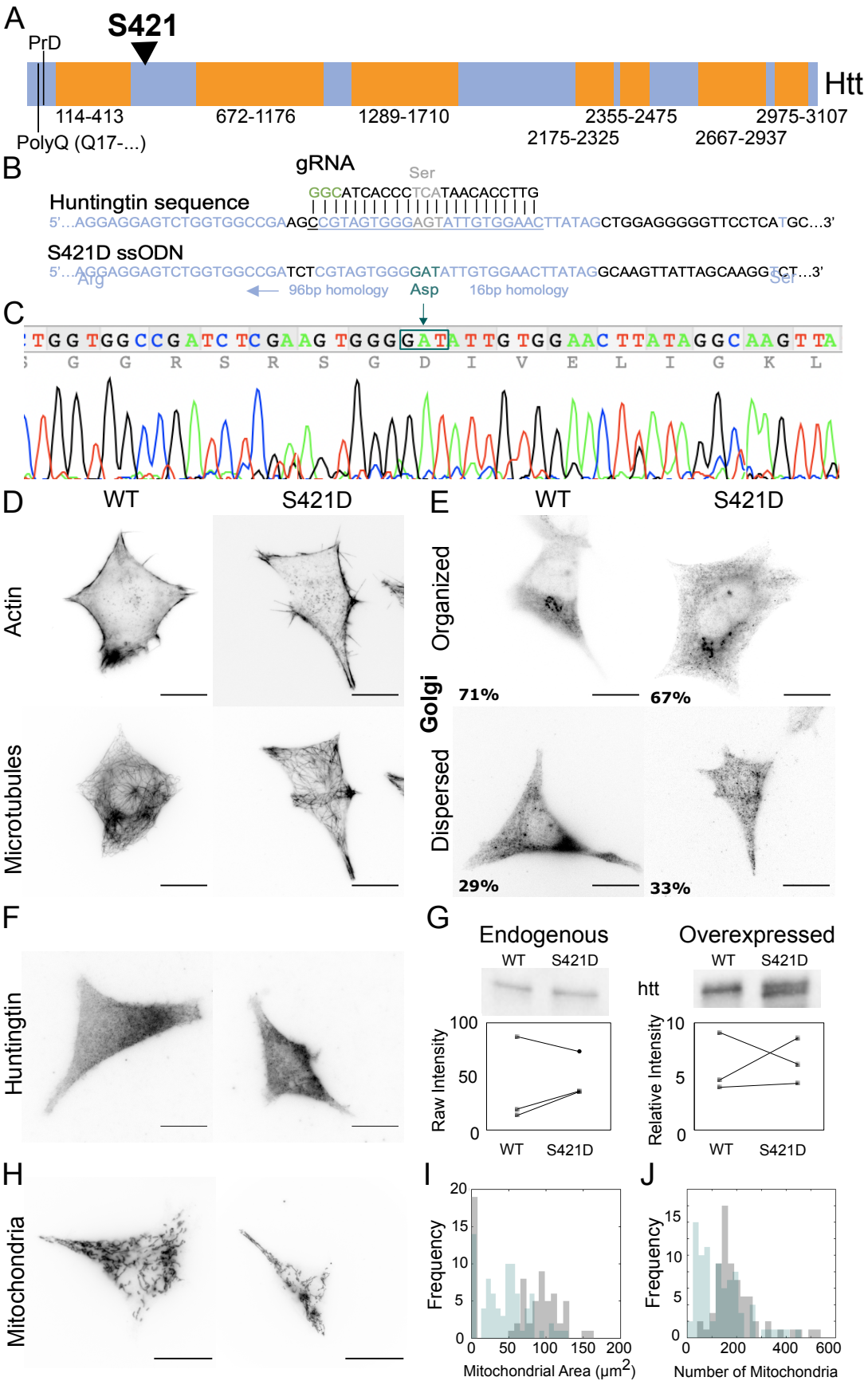
A
S421
PrD
Htt
114-413
672-1176
1289-1710
2355-2475
2975-3107
2175-2325
2667-2937
PolyQ (Q17-...)
B
gRNA
Ser
Huntingtin sequence
GGCATCACCCTCATAACACCTTG
5'...AGGAGGAGTCTGGTGGCCGAAGCCGTAGTGGGAGTATTGTGGAACTTATAGCTGGAGGGGGTTCCTCATGC...3'
S421D ssODN
5'...AGGAGGAGTCTGGTGGCCGATCTCGTAGTGGGGATATTGTGGAACTTATAGGCAAGGTCT...3'
Arg
96bp homology
Asp
16bp homology
Ser
C
D
WT
S421D
Actin
Microtubules
E
WT
S421D
Organized
Golgi
Dispersed
71%
67%
29%
33%
F
Huntingtin
G
Endogenous
Overexpressed
WT
S421D
htt
Raw Intensity
Relative Intensity
H
Mitochondria
I
Frequency
Mitochondrial Area (μm2)
J
Frequency
Number of Mitochondria

914

Fig. 1. S421D HEK293T cell line does not affect cytoskeletal organization, huntingtin localization, or dynein function. (A) Huntingtin protein sequence schematic demonstrating the structured domains (HEAT repeats and other α-helical regions, orange), unstructured domains (blue), S421 phosphosite, polyglutamine repeat region (PolyQ), and proline rich domain (PrD). (B) CRISPR phosphomimetic mutant design guide RNA (gRNA), and ssODN homologous recombination template. (C) Chromatogram of the positive clone containing the phosphomimetic mutation S421D. (D) Immunostaining of actin (top) and microtubules (bottom) indicating no difference between WT (left) and S421D (right) HEK293T cells. Note immunofluorescence images are inverted such that the protein of interest is dark, and the background is white, and all scale bars in the figure are 20 μm. (E) In both WT and S421D HEK293T cells, the Golgi apparatus appeared compact (organized) in ~70% of cells and dispersed in ~30% of cells. WT data for actin, microtubules, and Golgi apparatus staining was from 14 experiments, 84 cells, and S421D data from 11 experiments, 69 cells. (F) Immunofluorescence of huntingtin protein localization in WT (left) compared to S421D (right) HEK293T cells. Immunofluorescence of huntingtin localization for WT cells from 3 experiments, 43 cells and for S421D from 2 experiments, 22 cells. (G) WT and S421D huntingtin endogenous expression levels (top left) detected by Western blot with the raw intensity data from three independent samples (bottom left), compared to levels when overexpressing full length mCherry-WT or mCherry S421D huntingtin (top right) and the fold change relative to native expression levels for three independent samples (bottom right). Samples collected on the same date are connected by a line. (H) Mitochondrial morphology of WT (left) and S421D (right) HEK293T cells. (I) Mitochondrial area of WT (grey) compared to S421D (blue) cells, $p=6.59\times10^{-8}$ by Kolmogorov-Smirnov (ks) test. (J) Number of mitochondria per cell in WT (grey) compared to S421D (blue), $p=6.14\times10^{-7}$ by ks test. Mitochondrial analysis for WT from 7 experiments, 88 cells, and S421D from 7 experiments, 94 cells.

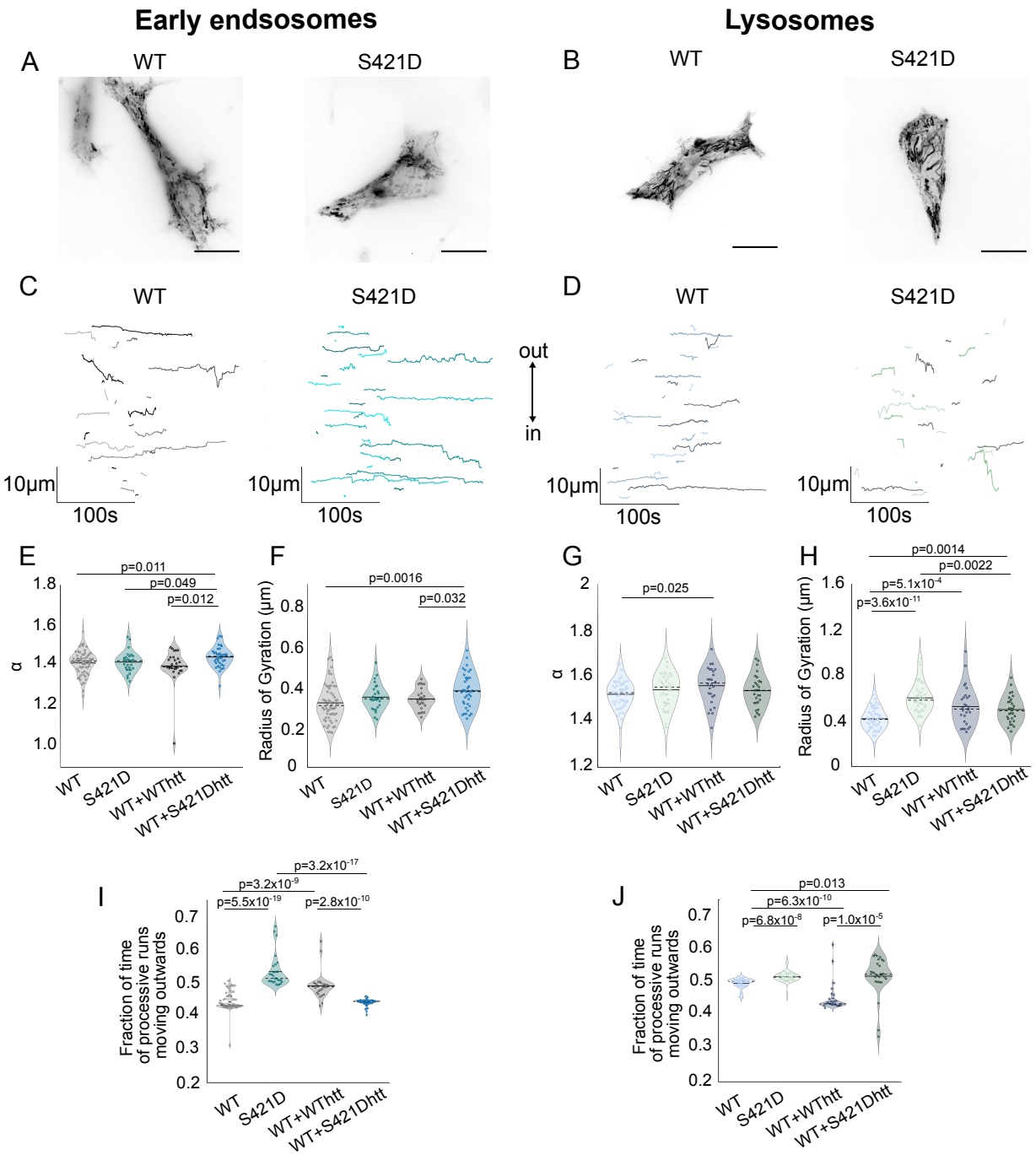

Fig. 2. Huntingtin S421D mutation increases outward motility of early endosomes and lysosomes while overexpression affects all parameters. (A, B) Maximum intensity projection of early endosomes, labelled with Rab5-eGFP, and lysosomes, labelled with Lysotracker, for endogenous WT and S421D huntingtin expressing cells. All scale bars are 20 µm. (C, D) Sample trajectories for early endosomes (C) and lysosomes (D) in both WT and S421D huntingtin endogenously expressing cells, with their inward (in) or outward (out) directionality indicated by the arrows in the center. Different shades of colours were assigned randomly to facilitate visualization of overlapping segments. (E, G) Early endosome (E) and lysosome (G) processivity per cell, measured by α, the slope of the log-log plot of their mean-squared displacement. Means are represented with a filled line, while medians are dashed lines. (F. H) Radius of gyration (R_g) per cell of early endosomes (F) and lysosomes (H). R_g is a measure of the radius that contains half of the datapoints in the trajectory centered around its average position. (I, J) Early endosome (I) and

949 lysosome (J) directional bias per cell of processive trajectories toward plus ends of microtubules (outwards),
950 the remaining fraction of processive trajectories move inwards. Overexpression conditions represented by
951 +WThtt or +S421Dhtt. Directional bias is determined by fraction of time particles are moving outwards
952 compared to inwards and averaged for each cell. The number of experiments, cells, and trajectories for
953 each condition are the following; WT early endosomes: 65 cells, 41994 trajectories, 6 experiments; S421D
954 early endosomes: 28 cells, 25476 trajectories, 3 experiments; WT+WThtt early endosomes: 28 cells, 17424
955 trajectories, 5 experiments, WT+S421Dhtt early endosomes: 39 cells, 22854 trajectories, 6 experiments;
956 WT lysosomes: 55 cells, 25247 trajectories, 5 experiments; S421D lysosomes: 38 cells, 12670 trajectories,
957 4 experiments; WT+WThtt lysosomes: 29 cells, 7558 trajectories, 5 experiments; WT+S421Dhtt lysosomes:
958 28 cells, 7031 trajectories, 6 experiments. Statistical significance was determined via Student's two-tailed
959 t-test and p-values are indicated on each plot where applicable.
960

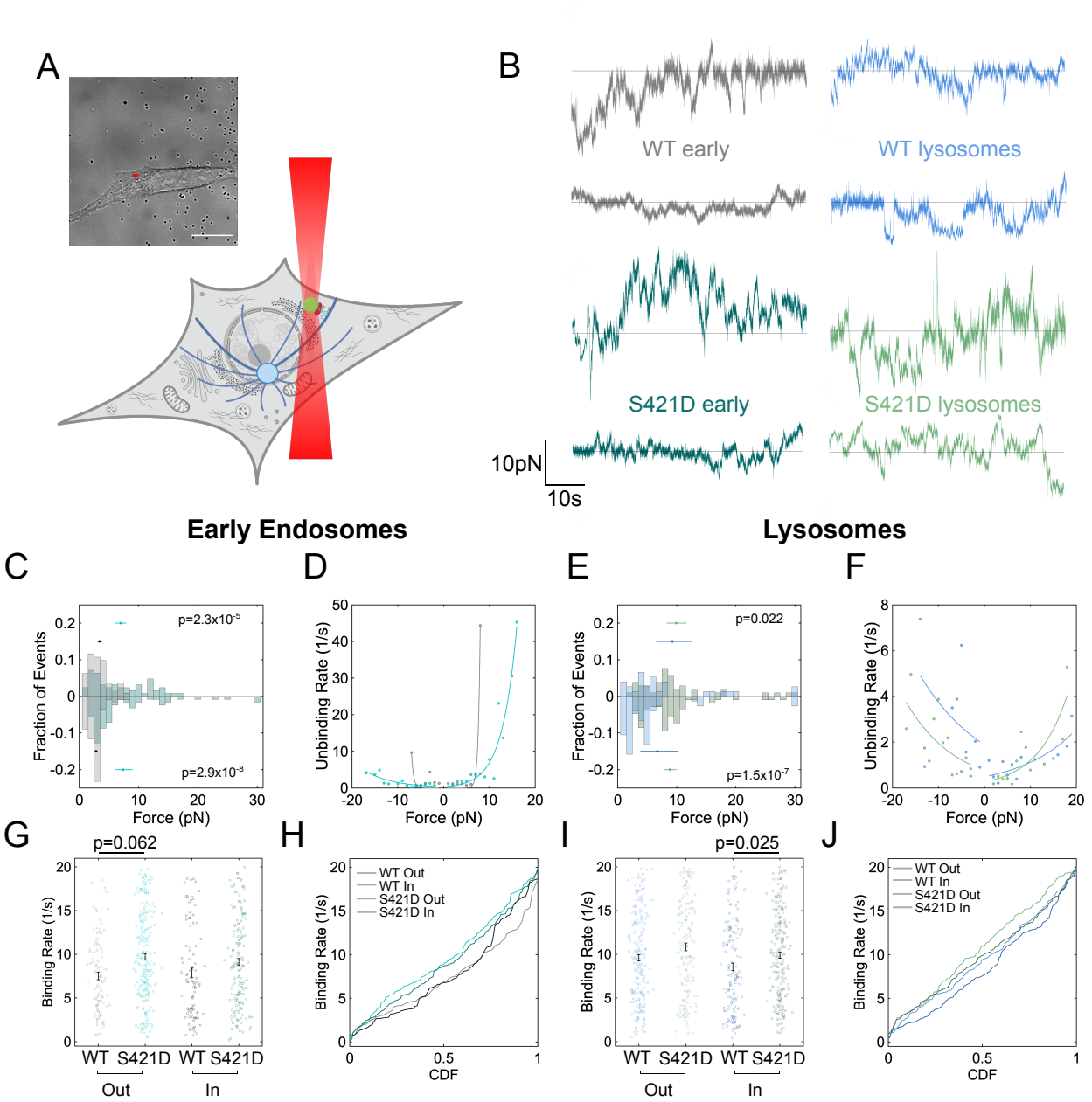

Fig. 3. Force trace analysis demonstrates S421D huntingtin induces higher binding rates, stronger binding, and higher forces in both directions for early endosomes and lysosomes. (A) Schematic of the optical tweezers assay including the endocytosed bead (green) inside the optical trap (red) along with a brightfield image of a cell during the experiment (top right). The scale bar is 20 μm and the arrowhead indicates the position of the optical trap during the experiment. (B) Sample force traces for early endosomes (early) and lysosomes in WT and S421Dhtt cells. The horizontal line indicates the zero axis, while positive values indicate outward forces and negative values indicate inward forces. (C, E) The fraction of early endosome or lysosome stall events at a given force with a minimum stall duration of 0.1 s, separated into 1 pN bins with the mean and 95% confidence intervals of bootstrap sampled means and p-values for each condition are shown above (for outward) or below (for inward) the distribution. The colours in (C-J) follow the colour legend from (B). (D, F) Force-dependent unbinding rates in both outward and inward directions (filled circles) for early endosomes or lysosomes fit with a single exponential (solid line). (G-J) Binding rates

for each stall event in early endosomes and lysosomes of WT and S421D in both directions in (G, I) including the cumulative distribution function (CDF) for each condition in (H, J). Statistical significance by ks test is indicated by the p-value in the figure panel where applicable. All results from optical tweezers data for WT early endosomes from 10 cells, 5 experiments; S421D early endosomes: 16 cells, 8 experiments; WT lysosomes: 12 cells, 5 experiments, S421D lysosomes: 11 cells, 4 experiments. Statistical significance was determined by ks test for binding rates and force distributions and p-values are indicated where applicable.

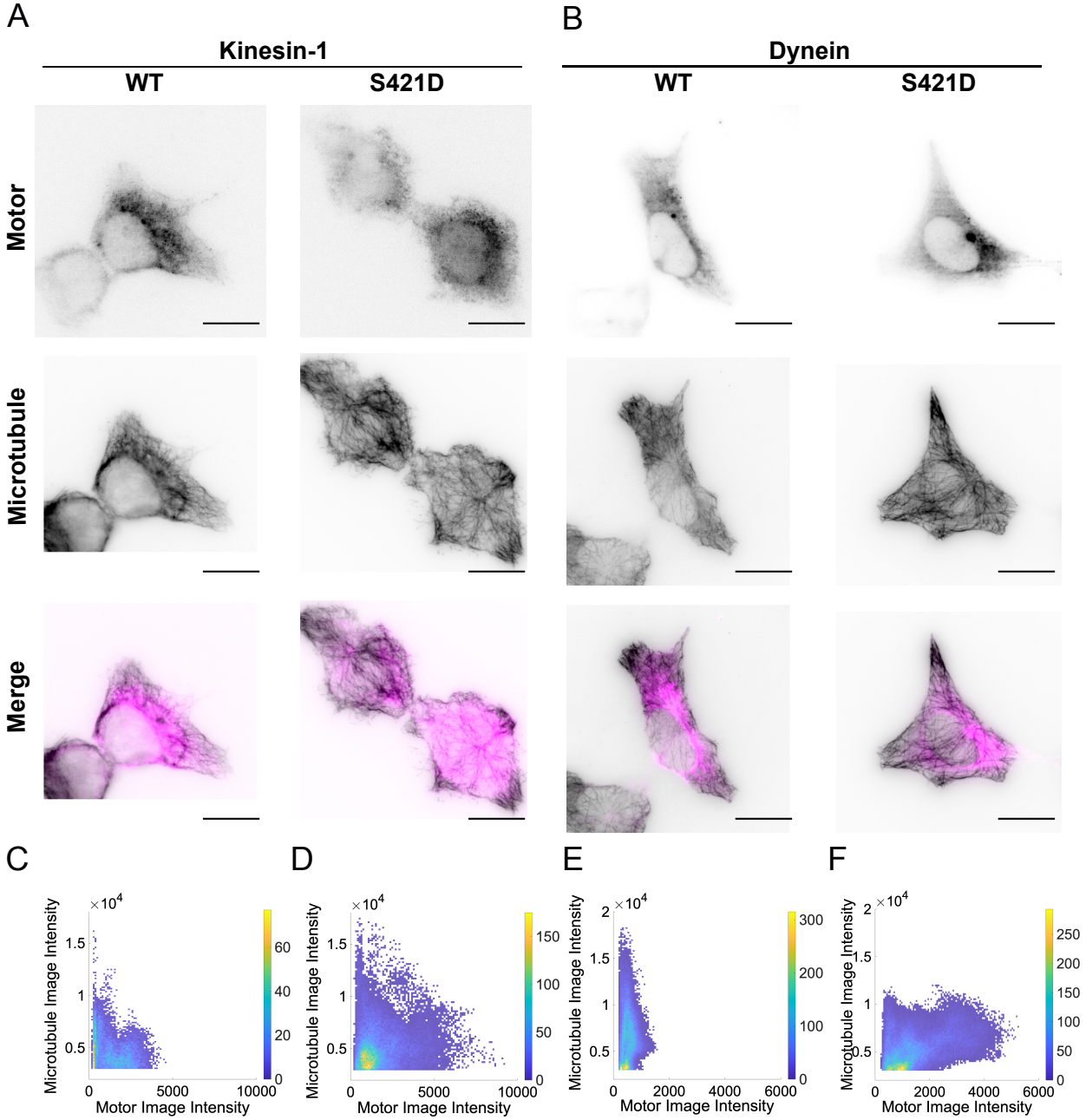

Fig. 4. S421D huntingtin increases kinesin and dynein association to extracted microtubules. (A, B) Inverted immunofluorescence images demonstrating colocalization (bottom) kinesin heavy chain (kinesin-1, (A), top) or dynein intermediate chain (dynein, (B), top) on extracted microtubules (middle) in WT and S421D huntingtin cells. In the merge channel, motors (kinesin-1 or dynein) are indicated in magenta and microtubules in black. All scale bars are 20 μm. (C-F) Colocalization plots were created from plotting intensity values of each pixel of the microtubule and motor (kinesin or dynein) channels of all images.

Differences between kinesin-1 WT and S421D correlation coefficients resulted in p=0.4748, while dynein WT compared to S421D correlation gave p=0.0533 by a two-tailed Student's t-test. Data for WT kinesin-1 from 17 cells, 3 experiments, S421D kinesin-1: 15 cells, 2 experiment, WT dynein: 32 cells, 4 experiments, and S421D dynein: 32 cells, 4 experiments.

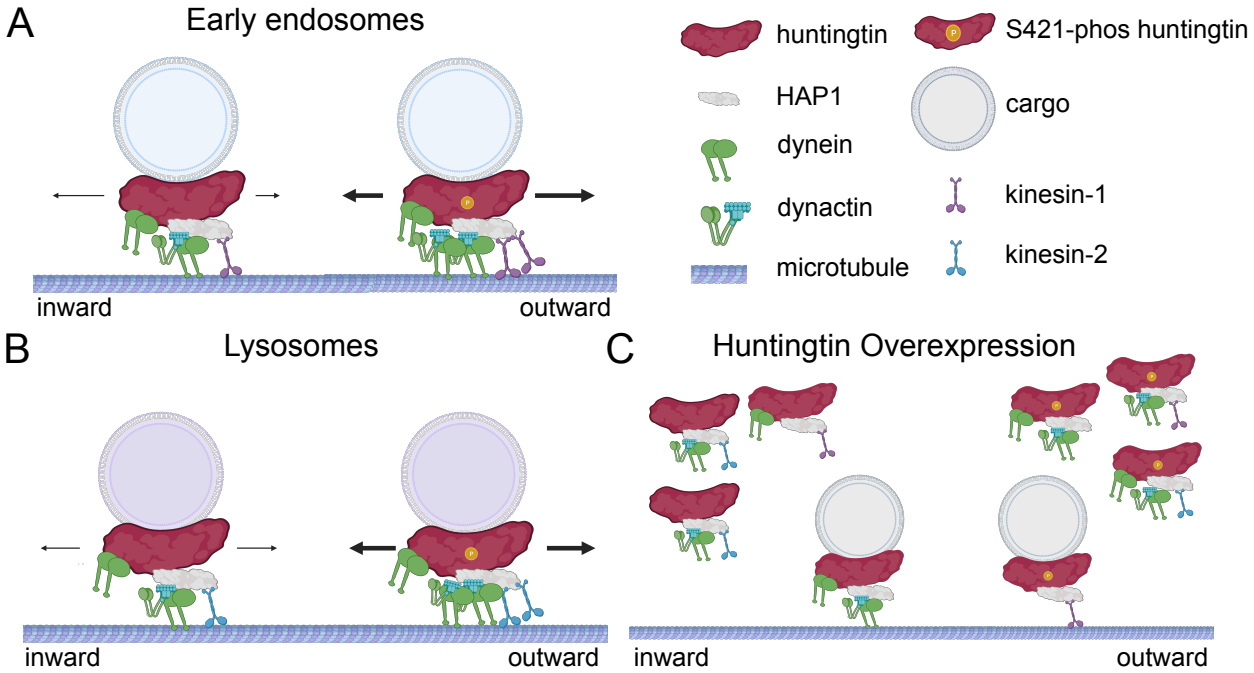

Fig. 5. Model of huntingtin S421 phosphorylation and expression level mediating regulation of early endosome and lysosome transport. (A) Huntingtin S421 phosphorylation (S421-phos) increases activity of kinesin and dynein motor proteins on early endosomes, such that the predominantly inward motility shifts to being more outward. (B) Lysosomes move bidirectionally. When kinesin and dynein activity are enhanced by huntingtin phosphorylation, the movement remains bidirectional, but the displacement of trajectories increases. (C) Overexpression sequesters motors and adaptors or disrupts vesicle-bound huntingtin-adaptor-motor complexes regardless of cargo identity or huntingtin phosphorylation state.

1004 ## SUPPLEMENTARY MATERIALS

1005

1006 **Table S1. Calculated parameters from exponential fits for unbinding rates of early endosomes and**
1007 **lysosomes.**

Condition	U_0	F_d (pN)
Early endosome WT outward	2.1×10^{-7}	0.42
Early endosome S421D outward	0.31	3.2
Early endosome WT inward	7.2×10^{-7}	0.43
Early endosome S421D inward	0.31	6.3
Lysosome WT outward	0.49	12.1
Lysosome S421D outward	0.24	6.6
Lysosome WT inward	1.9	14.6
Lysosome S421D inward	0.77	10.8

1008

1009

1010 **Movie S1. Live cell sample video of wild-type Rab5-eGFP early endosomes used for tracking**
1011 **analysis.** Image colours are inverted, the time scale is in seconds and frame rate is 10 fps, the scale bar
1012 is 20 μm.

1013

1014 **Movie S2. Live cell sample video of S421Dhtt Rab5-eGFP early endosomes used for tracking**
1015 **analysis.** Image colours are inverted, the time scale is in seconds and frame rate is 10 fps, the scale bar
1016 is 20 μm.

1017

1018 **Movie S3. Live cell sample video of wild-type LysoTracker™ lysosomes used for tracking analysis.**
1019 Image colours are inverted, the time scale is in seconds and frame rate is 10 fps, the scale bar is 20 μm.

1020

1021 **Movie S4. Live cell sample video of S421Dhtt LysoTracker™ lysosomes used for tracking analysis.**
1022 Image colours are inverted, the time scale is in seconds and frame rate is 10 fps, the scale bar is 20 μm.

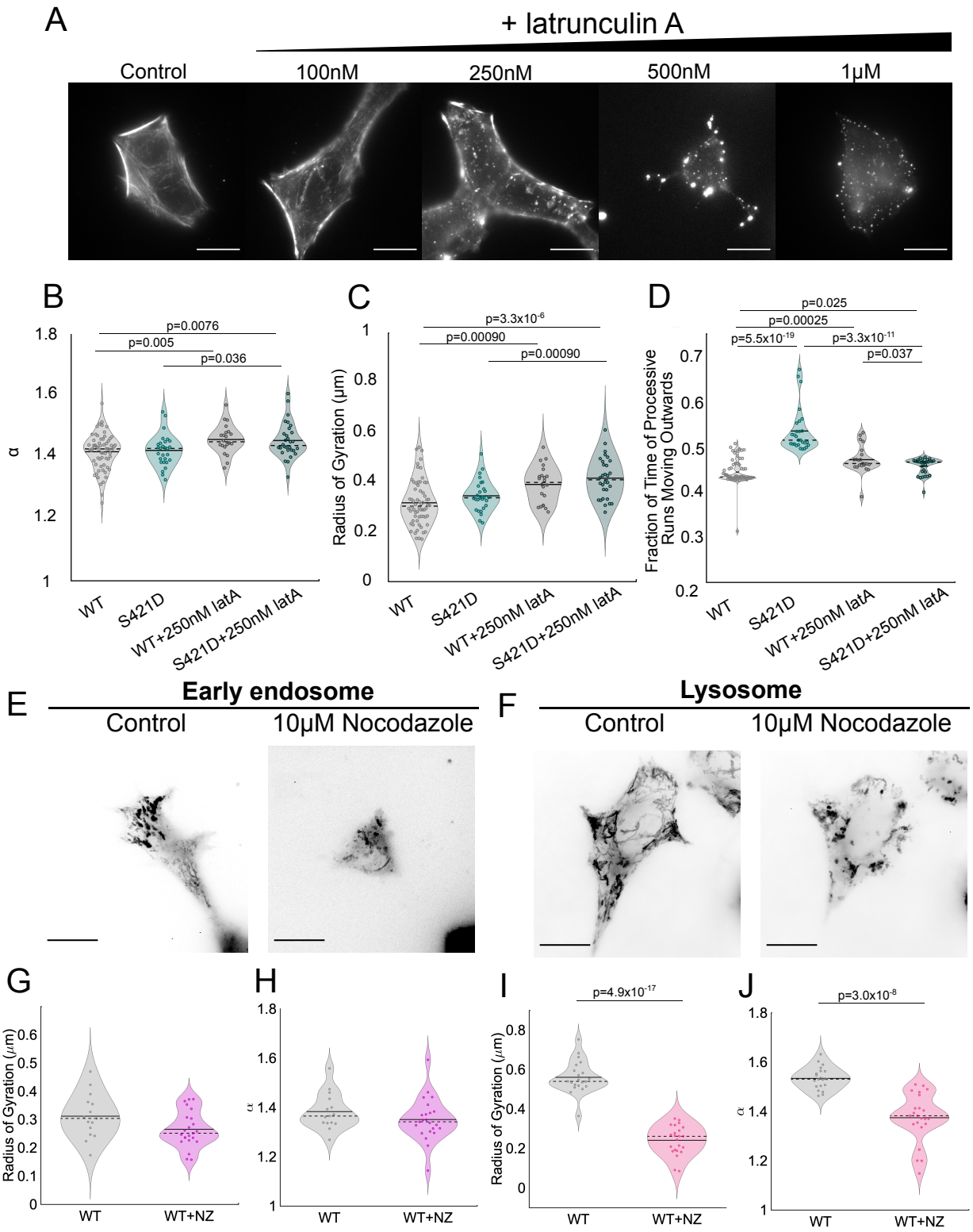

Fig. S1. Cytoskeletal disruption affects cargo motility. (A) Actin cytoskeleton labelled with SiR actin in S421D HEK293T cells treated with 100 nM-1 μM concentrations of latrunculin A (latA). Scale bars for all images are 20 μm, all images inverted. (B) Per cell α values of Rab5-eGFP labelled early endosomes. Means are represented with a filled line, while medians are dashed lines. (C) Radius of gyration (R_g) per cell is presented for early endosomes (C). (D) Directional bias per cell shown by fraction of time processive

1029 runs moving outward for Rab5-eGFP early endosomes. Note: control WT and S421D data for latrunculin A
1030 experiments is the same data reported in Fig. 2. (E, F) Maximum projections of the same cell with and
1031 without nocodazole (NZ) for early endosome and lysosome analysis. (G-J), Radius of gyration and alpha
1032 values for early endosomes and lysosomes before and after nocodazole treatment. (B-D) WT control data
1033 from 7 independent experiments (41994 trajectories, 64 cells), S421D data from 3 independent experiments
1034 (25476 trajectories, 28 cells), WT latA data from 3 independent experiments (17461 trajectories, 22 cells);
1035 S421D latA data from 5 independent experiments (19879 trajectories, 30 cells). (G, H) WT control data
1036 from 4 experiments, 22 cells, 6109 trajectories and WT+nocodazole data is from 4 experiments, 23 cells,
1037 and 7094 trajectories. (I, J) Contains control data from 4 experiments, 15 cells, 17073 trajectories, and
1038 nocodazole treated data from 4 experiments, 23 cells, and 6639 trajectories. Statistical significance of
1039 $p<0.05$ by Student's two sample t-test indicated in the figure where applicable.
1040

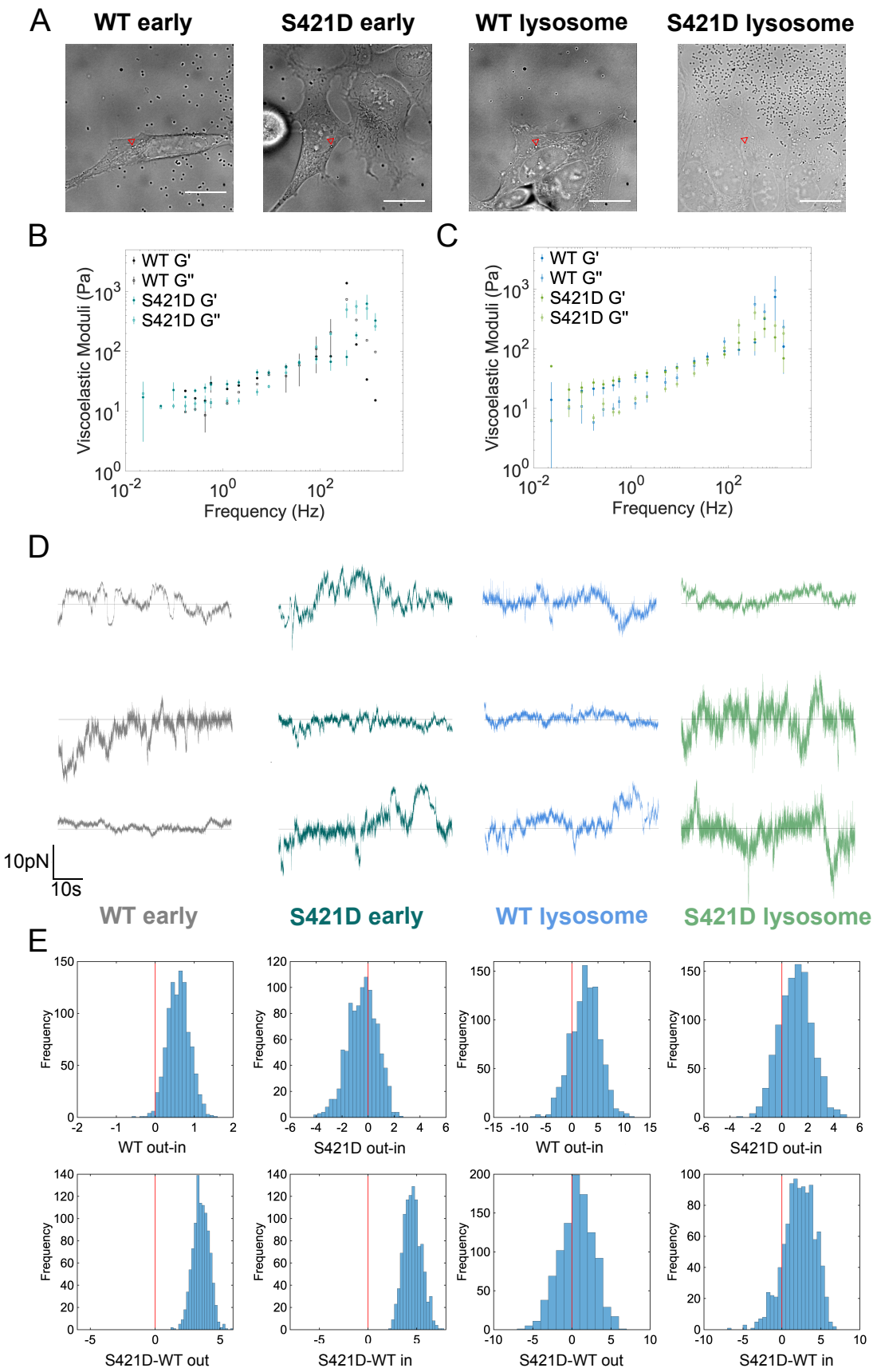
A
WT early
S421D early
WT lysosome
S421D lysosome
B
WT G'
WT G"
S421D G'
S421D G"
Viscoelastic Moduli (Pa)
Frequency (Hz)
C
WT G'
WT G"
S421D G'
S421D G"
Viscoelastic Moduli (Pa)
Frequency (Hz)
D
10pN
10s
WT early
S421D early
WT lysosome
S421D lysosome
E
Frequency
WT out-in
S421D out-in
WT out-in
S421D out-in
S421D-WT out
S421D-WT in
S421D-WT out
S421D-WT in

1041

Fig. S2. Force measurement analysis approach, additional force traces, and viscoelastic properties of WT and S421D huntingtin cells. (A) Brightfield image of a WT and S421D cell containing a trapped phagocytosed 500 nm bead (red arrow) during measurement of early endosome (early) or lysosome forces. (B, C) Viscous (G'') and elastic moduli (G') for WT (black) and S421D (teal) early endosomes and WT (blue) and S421D (green) lysosomes. (D) Additional sample force traces for each condition in optical tweezers assays, the horizontal line indicates the zero axis. Positive value forces are directed outward and negative forces are directed inward. (E) Distributions of bootstrap mean differences evaluated for additional statistical analysis of force distributions for the differences shown on the x axis of each plot in both early (left) and late (right) endosomes.

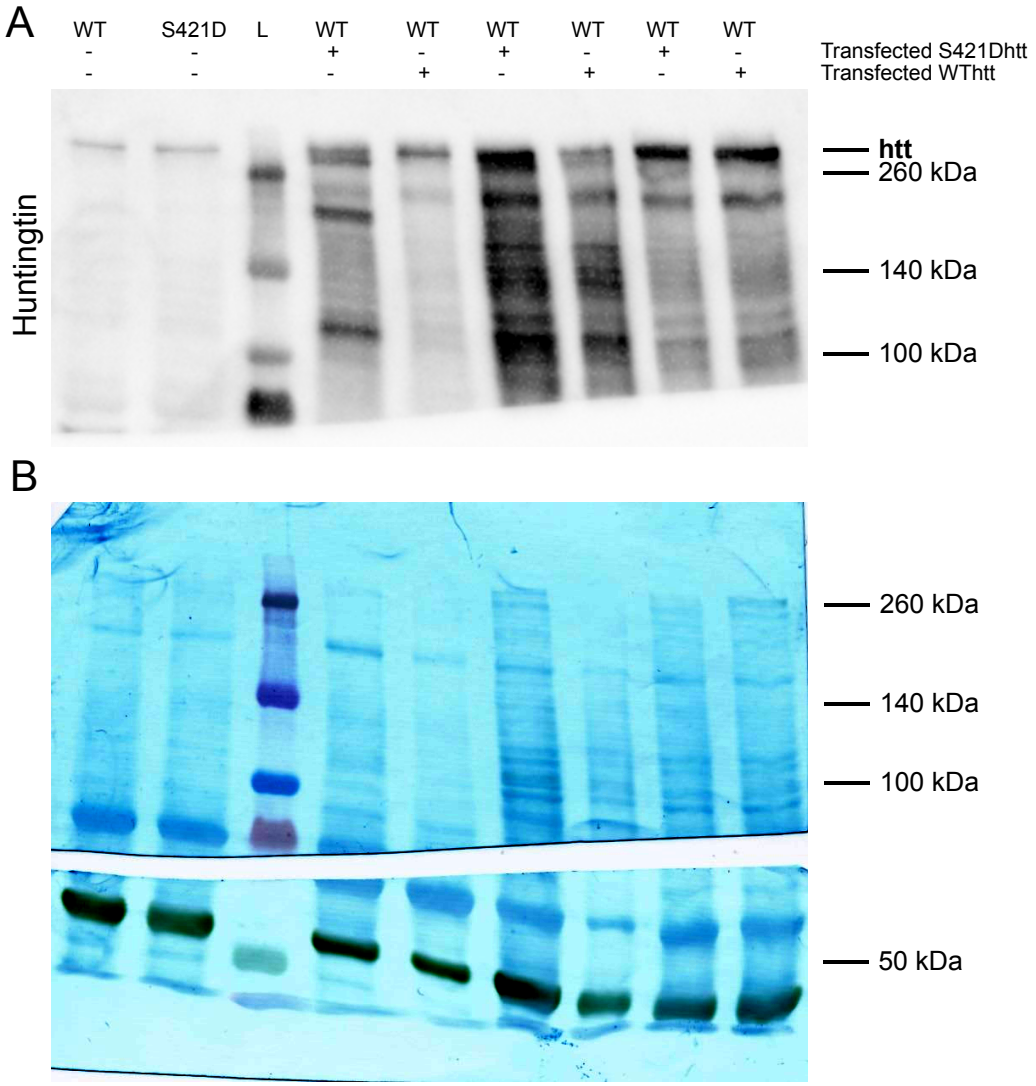

Fig. S3. Western blot transparency for huntingtin blot in Fig. 1. (A) Full western blot (above 100 kDa) of the blot presented in Fig. 1G using the anti-huntingtin antibody. Ladder is indicated by L with molecular weights to the right of the blot. (B) Coomassie staining of the entire membrane post-antibody staining.